Chapter 10

FEMTOSECOND PLASMA-MEDIATED NANOSURGERY OF CELLS AND TISSUES

Alfred Vogel[1], Joachim Noack[1], Gereon Hüttman[1] and Günther Paltauf[2]
[1]Institut für Biomedizinische Optik, Universität zu Lübeck, Peter-Monnik Weg 4, D-23562 Lübeck, Germany; [2]Institut für Physik, Karl-Franzens-Universität Graz, Universitätsplatz 5, A-8010 Graz, Austria

1. INTRODUCTION

1.1 Cell surgery

Nonlinear absorption of short and ultrashort laser pulses focused through microscope objectives of high numerical aperture (NA) can be used to achieve very fine and highly localized laser effects inside of biological media that are transparent at low irradiance (Shen, 1984, Vogel and Venugopalan, 2003, Venugopalan et al., 2002, König et al., 1999, Vogel et al., 2005) as well as in the bulk of photonic materials (Shaffer et al., 2001, Minoshima et al., 2001).

With moderate NAs and nanosecond laser pulses, this possibility has been utilized already in the 1980s for intraocular surgery (Steinert and Puliafito, 1986, Vogel et al., 1986). After the advent of femtosecond lasers, it was employed also for corneal intrastromal refractive surgery (Ratkay-Traub et al., 2003, Heisterkamp et al., 2003) and for the creation of corneal flaps in excimer laser refractive surgery (LASIK) (Juhasz et al., 1999, Ratkay-Traub et al., 2003, Heisterkamp et al., 2003, Han et al., 2004). However, with moderate NAs, the spatial distribution of the deposited energy is influenced by nonlinear self-focusing, normal group velocity dispersion, and plasma-defocusing leading to filamentation and streak formation in the biological material (Shen, 1984, Vogel et al., 1996a, Heisterkamp et al., 2002, Liu et al., 2003, Kasparian et al., 2004, Kolesik et al., 2004, Arnold et al., 2005) The nonlinear propagation effects become ever more important when the laser pulse duration is reduced and a larger laser power is required to produce optical breakdown. Therefore, it is not possible to achieve highly localized energy deposition when femtosecond pulses are focused into the bulk of transparent

media at low NA. With increasing numerical aperture the spot size becomes smaller and thus the power that is necessary to overcome the threshold irradiance decreases. Beyond a certain numerical aperture, the breakdown power is smaller than the critical power for self-focusing, and localized energy deposition on a sub-micrometerscale can be achieved. For femtosecond optical breakdown in water and glass this was found to be the case for NA ≥ 0.9 (Schaffer et al., 2001).

Recent years have seen a continuous rise of interest in micro- and nanosurgery on a cellular and subcellular level. One important application is the separation of individual cells or other small amounts of biomaterial from heterogeneous tissue samples for subsequent genomic or proteomic analysis. Sensitive analytical techniques such as polymerase chain reaction (PCR) enable the analysis of very small amounts of materials, which allows for ever more specific investigations of cell constituents and their function. Key technologies for sample preparation are laser microdissection (LMD) (Meier-Ruge et al., 1976) and subsequent laser pressure catapulting (LPC) of the dissected specimens into a vial for further analysis (Schütze and Lahr, 1998, Schütze et al., 1998, Niyaz and Sägmüller, 2005). A related technique is laser-induced cell lysis and catapulting of the cell content into a micropipet for time-resolved capillary electrophoresis (Sims et al., 1998). Laser microbeams have also been applied to dissect chromosomes (Berns et al., 1981, Liang et al., 1993, Greulich, 1999, König et al., 2001), and fuse cells (Schütze and Clement-Sengwald, 1994). Laser-induced transient permeabilisation of the cell membrane is of great interest for a gentle transfection of genes and transfer of other substances into specific cell types (Tsukakoshi et al., 1984, Tao et al., 1987, Krasieva et al., 1998, Soughayer et al., 2000, Tirlapur and König, 2002, Zeira et al., 2003, Paterson et al., 2005.

Laser-generated inactivation of specific proteins or cell organelles together with an analysis of the induced deviations from the normal development provides information about the function of the respective proteins and organelles and can be utilized to study cell proliferation, embryonal development, or stress-induced reaction pathways. Two complementary strategies for functional studies have been followed. In the ‘systemic’ approach, specific proteins or DNA sequences are targeted by means of antibodies attached to metallic nanoparticles or chromophores (Huettmann and Birngruber, 1999, Jay and Sakurai, 1999, Pitsillides et al., 2003, Yao et al., 2005, Garwe et al., 2005). When the antibody-absorber conjugates have bound to the target protein(s), the entire cell or group of cells is exposed to a short-pulsed laser beam. Protein inactivation occurs through linear absorption of the laser irradiation in the nanoparticles or chromophores, respectively, resulting in thermo-mechanical or photochemical destruction of the target proteins regardless of their localisation within the cell. Alternatively, in the ‘local’ approach,

which is investigated in the present paper, one or a few specific target structures are irradiated by a tightly focused laser beam. As the laser energy is deposited via non-linear absorption, surgery can be performed at any desired location within a cell or a small organism, regardless of their linear absorption properties.

1.2 Historical development

Historically, light inactivation of cells or cell organelles was first attempted in 1912 by Tschachotin using 280-nm irradiation from a magnesium spark imaged by a microscope objective on a 5 μm wide spot on the cell (Tschachotin, 1912). This type of apparatus was in the 1950s highly refined by Bessis and Nomarski (1960), and the resolution increased into the sub-micrometer regime. However, these instruments required very long exposure times. After the advent of the laser, a high-brightness light source was available that enabled to reduce the exposure time into the microsecond range (Bessis et al., 1962). First experiments on mitochondrial inactivation were performed using free-running ruby laser pulses with about 500 μs duration that were focused into a 5 μm spot (Amy and Storb, 1965). Later, chromosomal dissection was demonstrated using argon laser irradiation with 20-30 μs duration (Berns et al., 1969, 1971). Owing to the good quality of the argon laser beam and the shorter wavelength, it could be focused into a much smaller spot than the multimode emission of the initial ruby lasers. It is important to note that microsecond pulses are still 'long' in the context of cell surgery because during pulses longer than about 10 μs a stationary temperature distribution similar to that produced by continuous wave (cw) irradiation evolves around the laser focus (Vogel et al., 2005).

Soon researchers began to use also short-pulsed laser irradiation, mostly with wavelengths in the UV region of the optical spectrum and with durations of a few nanoseconds (Bessis, 1971, Meier-Ruge et al., 1976, Berns et al., 1981, Schütze and Clement-Sengwald, 1994, Krasieva et al., 1998, Greulich, 1999, Colombelli et al., 2004, Colombelli et al., 2005a,b). It was found that short laser pulses enable localized energy deposition at arbitrary locations without external sensitizing agents, even though the ablation threshold can still be lowered by staining of the target structures. With nanosecond pulses, energies between 0.25 μJ and 250 μJ were required to produce the desired ablative effect, depending on the laser wavelength, beam profile, numerical aperture, and the quality of the optical scheme used for coupling the laser beam into the microscope. Use of UV wavelengths that are well absorbed by biomolecules yielded lower ablation thresholds than the use of visible or near IR irradiation under similar focusing conditions. Recently, it was demonstrated that pulsed laser microdissection relies on plasma formation supported by

linear absorption, and that this is associated with violent mechanical effects (shock wave emission and cavitation bubble formation) reaching well beyond the region of energy deposition (Venugopalan et al., 2003). Pulse energies in the microjoule range typical for nanosecond laser microbeams can therefore severely affect the cell viability.

In search for finer effects, researchers employed first picosecond pulses that could produce intracellular dissections with energies of 70-140 nJ (Liang et al., 1993), and later femtosecond pulses that enabled to lower the ablation threshold to an energy range between 0.4 nJ and a few nanojoules (König et al., 1999, Yanik et al., 2004). Due to the low energy threshold for plasma formation (Vogel et al., 1999, Noack and Vogel, 1999), femtosecond pulses can create very fine effects with a spatial extent below the optical diffraction limit. This has been demonstrated in chromosomes (König et al., 1999, König et al., 2001), various other cell organelles (Meldrum et al., 2003, Watanabe et al., 2004, Heisterkamp et al., 2005, Sacconi et al., 2005, Shen et al., 2005), small organisms (Yanik et al., 2004, Supatto et al., 2005a,b, Chung et al., 2005), and tissues (König et al., 2002, Zeira et al., 2003, Riemann et al., 2005). Sub-diffraction limited resolution can be achieved because the nonlinear absorption diminishes the volume into which the laser energy is deposited. While for nanosecond pulses the optical breakdown threshold depends strongly on the linear absorption at the laser focus, femtosecond optical breakdown exhibits a much weaker dependence on the absorption coefficient of the target material (Oraevsky et al., 1996). This facilitates the targeting of arbitrary cellular structures. Because the wavelength dependence of femtosecond breakdown is weak (Vogel and Noack, 2001), IR wavelengths that can penetrate deeply into the tissue can be used without compromising the precision of tissue effects as observed with ns pulses (Krasieva et al., 1998, Venugopalan et al., 2002). Moreover, when pulses from a femtosecond oscillator are used, it becomes possible to combine nonlinear material modification with nonlinear imaging techniques based on 2-photon fluorescence excitation or second harmonic generation (König et al., 2002, Tirlapur and König, 2002, Yanik et al., 2004, König et al., 2005, Saccioni et al.., 2005, Supatto et al., 2005a,b). Additional progress was possible through the use of modern gene fusion products such as green fluorescent proteins (GFP) which permit the visualization and ablation of cellular structures that are below the resolution of a light microscope (Botvinick et al., 2004, Yanik et al., 2004, Supatto et al., 2005a,b). The above advances allow for an unprecedented precision of aiming, surgery, and of the analysis of the created immediate and long-term effects. This potential of fs and ps pulses has been utilized in a variety of functional studies to elucidate the mechanisms of chromosome separation during cell division (Liang et al., 1993, Grill et al., 2003), induce highly localized DNA damage (Meldrum et al., 2003), measure the biophy-

sical properties of the cytoskeleton and mitochondria (Shen et al., 2005, Colombelli et al., 2005b, Maxwell et al., 2005), stimulate calcium waves in living cells (Smith et al., 2001), demonstrate nerve regeneration after axotomy within a living C. elegans worm (Yanik et al., 2004), map thermosensation in C. elegans (Chungs et al., 2005), and to shed light on morphogenetic movements in embryonal development (Berns et al., 1981, Supatto et al., 2005a,b).

1.3 Objectives of the present study

The high precision of the femtosecond laser effects is certainly related to the fact that the energy threshold for femtosecond optical breakdown is very low. The low breakdown threshold is, however, not sufficient to explain the fineness of the laser effects because laser-induced breakdown is generally associated with mechanical effects such as shock wave emission and bubble formation that extend beyond the focal region (Vogel et al., 1996b, Venugopalan et al., 2002). We found in previous theoretical studies that plasmas with a large free electron density are produced in a fairly large irradiance range below the breakdown threshold that was defined by a critical free electron density $\rho_{cr} = 10^{21}$ cm^{-3} (Vogel and Noack, 2001, Vogel et al., 2002). To understand the full potential of femtosecond pulses for highly localized material processing and modification of biological media, one therefore needs to include the irradiance range *below* the optical breakdown threshold. Moreover, one needs to elucidate why the conversion of absorbed laser light into mechanical energy above the breakdown threshold is much smaller than for longer pulse durations (Vogel et al., 1999, Vogel and Venugopalan, 2003).

The present study investigates the chemical, thermal, and thermomechanical effects arising from low-density plasmas to explain the mechanisms underlying femtosecond-laser nanosurgery of cells and biological tissues. One technique for nanosurgery uses long series of pulses from fs oscillators with repetition rates in the order of 80 MHz and pulse energies well below the optical breakdown threshold that do not much exceed the energies used for nonlinear imaging (König et al., 1999, König et al., 2001, Tirlapur and König, 2002, Zeira et al., 2003, Saccioni et al., 2005, Supatto et al., 2005a,b, König et al., 2005). The other approach uses amplified pulse series at 1 kHz repetition rate with pulse energies slightly above the threshold for transient bubble formation (Yanik et al., 2004, Watanabe et al., 2004, Heisterkamp et al., 2005, Shen et al., 2005). To cover both parameter regimes, we investigate plasma formation and plasma-induced effects for an irradiance range reaching from the values used for nonlinear imaging to those producing bubble formation. We consider repetition rates in the kilohertz range where the mechanical and thermal events induced by subsequent pulses are largely independent, and in the megahertz range where accumulative effects are likely to occur.

We use a rate equation model considering multiphoton ionization, tunnel ionization, and avalanche ionization to numerically simulate plasma formation. The value of the energy density created by each laser pulse is then used to calculate the temperature distribution in the focal region after application of a single laser pulse and of series of pulses. The results of the temperature calculations yield, finally, the starting point for calculations of the thermoelastic stresses that are generated during the formation of the low-density plasmas, and of stress-induced bubble formation. All calculations are performed for a numerical aperture of NA = 1.3 and the wavelength of the titanium sapphire laser (λ = 800 nm). Where possible, the findings of the numerical simulations are compared to experimental results.

2. MODELING OF PLASMA FORMATION

The process of plasma formation through laser-induced breakdown in transparent biological media is schematically depicted in Fig. 1. It essen tially consists of the formation of quasi-free electrons by an interplay of photoionization and avalanche ionization.

It has been shown experimentally that the optical breakdown threshold in water is very similar to that in ocular and other biological media (Docchio et al., 1986). For convenience, we shall therefore focus attention on plasma formation in pure water. Whereas the optical breakdown in gases leads to the generation of free electrons and ions, in condensed matter electrons are either bound to a particular molecule or they are "quasi-free" if they have sufficient

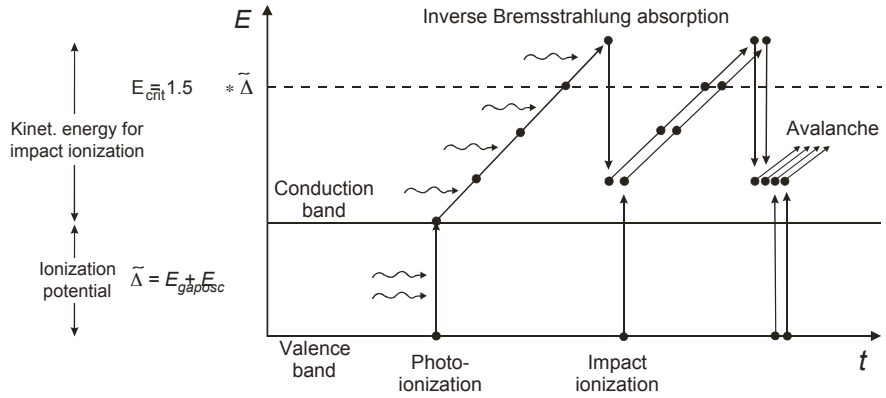

Figure 1: Interplay of photoionization, inverse Bremsstrahlung absorption and impact ionization in the process of plasma formation. Recurring sequences of inverse Bremsstrahlung absorption events and impact ionization lead to an avalanche growth in the number of free electrons. The consequences of the conservation laws for energy and momentum on the energetics of impact ionization are discussed in the text.

kinetic energy to be able to move without being captured by local potential energy barriers. Transitions between bound and quasi-free states are the equivalent of ionization of molecules in gases. To describe the breakdown process in water, Sacchi (1991) has proposed that water should be treated as an amorphous semiconductor and the excitation energy Δ regarded as the energy required for a transition from the molecular $1b_1$ orbital into an excitation band (band gap 6.5 eV) (Grand et al., 1970, Nikogosyan et al., 1983). We follow this approach. For simplicity, we use the terms "free electrons" and "ionization" as abbreviations for "quasi-free electrons" and "excitation into the conduction band". Nonlinear absorption processes of liquid water do actually not only consist of ionization but also include dissociation of the water molecules (Nikogosyan et al., 1983). However, in our model dissociation is neglected to reduce the complexity of the numerical code.

The excitation energy into the conduction band can be provided either by photoionization (multiphoton ionization or tunneling (Keldysh, 1965, Ammosov et al., 1986), or by impact ionization (Shen, 1984, Thornber, 1981, Arnold and Cartier, 1992, Ridley, 1999). In previous breakdown models, it was often assumed that a free electron could be produced as soon as the band gap Δ was exceeded either by the sum of the simultaneously absorbed photons, or by the kinetic energy of an impacting free electron (kennedy, 1995, Feng et al., 1997, Noack and Vogel, 1999, Tien et al., 1999). However, for very short laser pulses where breakdown occurs at large irradiance values, the band gap energy has to be replaced by the effective ionization potential to account for the oscillation energy of the electron due to the electric laser field. The ionization potential of individual atoms is (Keldysh, 1965)

$$\widetilde{\Delta} = \Delta + e^2 F^2 / (4m\omega^2) , \tag{1}$$

where ω and F denote the circular frequency and amplitude of the electric laser field, e is the electron charge, and $1/m = 1/m_c + 1/m_v$ is the exciton reduced mass that is given by the effective masses m_c of the quasi-free electron in the conduction band and m_v of the hole in the valence band. The second term in equation (1) can be neglected in nanosecond optical breakdown but must be considered in femtosecond optical breakdown where F is orders of magnitude larger. For condensed matter, the description of the ionization potential is more complex than Eq. (1) (Keldysh, 1965, Vogel et al., 2005).

Multiphoton ionization (MPI) and tunneling are the mechanisms governing photoionization for different field strengths and frequencies of the electromagnetic field. In his classical paper, Keldysh (1965) introduced a parameter $\gamma = \omega / \omega_t$ to distinguish tunneling and MPI regimes. Here $1/\omega_t$ stands for the tunneling time through the atomic potential barrier which is inversely

proportional to the strength of the electromagnetic field. For values $\gamma << 1$ as obtained with low frequencies and large field strengths tunneling is responsible for ionization, while for values $\gamma >> 1$ typical for optical frequencies and moderate field strengths the probability of MPI is much higher than that of tunneling. However, femtosecond optical breakdown requires very high field strengths for which the tunneling time through the atomic potential barrier is extremely short, leading to values $\gamma < 1$ of the Keldysh parameter even for optical frequencies (Tien et al., 1999). Approximations of the Keldysh theory considering only multiphoton ionization that were used in previous breakdown models (Kennedy, 1995, Feng et al., 1997, Nock and Vogel, 1999) are thus inappropriate for the modeling of femtosecond breakdown, especially for pulse durations ≤ 100 fs.

Once a free electron is produced in the medium, it can absorb photons in a non-resonant process called "inverse Bremsstrahlung" in the course of collisions with heavy charged particles (ions or atomic nuclei). A third particle (ion/atom) is necessary for energy and momentum to be conserved during absorption, as they cannot both be conserved if only an electron and a photon interact. The electron gains kinetic energy during the absorption of the photon. After a sequence of several inverse Bremsstrahlung absorption events, the kinetic energy is sufficiently large to produce another free electron through impact ionization (Thornber, 1981, Arnold and Cartier, 1992, Ridley, 1999, Kaiser et al., 2000). Two free electrons with low kinetic energies are now available which can gain energy through inverse Bremsstrahlung absorption (Fig. 1). The recurring sequence of inverse Bremsstrahlung absorption events and impact ionization leads to an avalanche growth in the number of free electrons if the irradiance is high enough to overcome the losses of free electrons through diffusion out of the focal volume and through recombination. The energy gain through inverse Bremsstrahlung must, moreover, be more rapid than the energy loss by collisions with heavy particles occurring without simultaneous absorption of a photon (the fraction of energy lost is proportional to the ratio of the electron and ion masses). The whole process is called "avalanche ionization", or "cascade ionization".

For impact ionization to occur, the kinetic energy of the impacting electron must be larger than the effective ionization potential $\tilde{\Delta}$ to satisfy the conservation laws for energy and momentum (Keldysh, 1960, Ridley, 1999). According to Ridley (1999), the critical energy for bands with parabolic energy dispersion is

$$E_{crit} = \left[(1+2\mu)/(1+\mu)\right]\tilde{\Delta}, \quad \text{with } \mu = m_c/m_v. \tag{2}$$

The value of μ depends on the band structure, it is 1 for a symmetric band structure with the Fermi level at the center of the band gap but smaller for

semiconductors (Ridley, 1999). Kaiser et. al. (2000) assumed $\mu = 1$ for α-SiO_2, and since we did not find information on the value of μ for water, we follow their assumption. This implies that a kinetic energy of $E_{crit} = 1.5\,\tilde{\Delta}$ is required for impact ionization (Kaiser et al., 2000, Rethfeld, 2004).

The excess energy of $0.5\,\tilde{\Delta}$ that remains after impact ionization is distributed among the collision partners. Thus, each quasi-free electron produced by impact ionization has to gain less energy than $1.5\,\tilde{\Delta}$ to reach the critical energy. However, the average energy leading to an impact ionization event is larger than E_{crit} because the impact ionization rate increases with kinetic energy (Keldysh, 1960, Arnold and Cartier, 1992, Kaiser et al., 2000, Rethfeld, 2004). To consider both factors, we assume that the average energy gain required for a free electron to cause impact ionization is $1.5\,\tilde{\Delta}$, as illustrated in Fig. 1.

While strong-field ionization is almost "instantaneous," there are time constraints on cascade ionization because several consecutive inverse Bremsstrahlung absorption events are necessary for a free electron to pick up the critical energy for impact ionization. For a band gap of 6.5 eV in water and a Keldysh parameter $\gamma = 2$, the effective ionization potential is $\tilde{\Delta} \approx 7.3$ eV, and the average gain in kinetic energy required to enable impact ionization is $(3/2)\,\tilde{\Delta} \approx 10.95$ eV. When laser irradiation of $\lambda = 800$ nm wavelength with a photon energy of 1.55 eV is used to produce optical breakdown, an electron must undergo at least $n = 8$ inverse Bremsstrahlung absorption events before impact ionization can occur. As mentioned above, inverse Bremsstrahlung absorption can only occur during collisions of the electrons with heavy particles. In condensed matter, the time τ between collisions was estimated to be roughly 1 fs (Bloembergen, 1984). Recent experimental investigations yielded a value of $\tau = 1.7$ fs for fused silica (Sun et al., 2005). Based on this value, the minimum time for one doubling sequence of the number of free electrons by cascade ionization is $\tau_{\mathrm{ion}} = \tau\, n = 13.6$ fs, even if every collision involves absorption of a photon. A detailed analysis of the time constraints in cascade ionization was presented by Kaiser et. al. (2001) and Rethfeld (2004). They come to the conclusion that cascade ionization plays only a minor role in femtosecond breakdown compared to multiphoton effects – in striking contrast to Joglekar et. al. (2004) who present some experimental evidence for the opposite statement.

In our study, we shall combine the complete Keldysh model for strong-field ionization (Eq. (38) in Keldsh's paper (1965)) with the description of avalanche ionization used by Shen (1984), Kennedy (1995), and Stuart et al. (1996), which is based on the Drude model. Since the numerical model used by Kaiser et. al. (2000) and Rethfeld (2004) is very complex we consider the time constraints in cascade ionization in a simpler way by evaluating the

contribution of cascade ionization at time t using the electron density created at the retarded time $t_{\mathrm{ret}} = t - t_{\mathrm{ion}}$ (Vogel et al., 2005).

In most theoretical investigations, the electron density

$$\rho_{cr}^{'} = \omega^2 (m_c \, \varepsilon_0 / e^2) \tag{3}$$

above which the plasma becomes both strongly reflective and absorbing is used as breakdown criterion (Stuart et al., 1996, Lenzner et al., 1998, Tien et al., 1999, Kaiser et al., 2000, Mao et al., 2004). Here ε_0 denotes the vacuum dielectric permittivity. We use a free electron density of $\rho_{\mathrm{cr}} = 10^{21}$ cm^{-3} as breakdown criterion, which is close to ρ_{cr} for $\lambda = 1064$ nm. The experimental threshold criterion is bubble formation. Plasma luminescence, which is often used as threshold criterion for nanosecond breakdown, is not or only with great difficulties detectable for ultrashort laser pulses (Hammer et al., 1996, Noack and Vogel, 1999).

Since all calculations are performed for a numerical aperture of NA = 1.3, nonlinear propagation effects in the biologic medium can be neglected even for pulse durations as short as 100 fs because Schaffer et. al. (2001) showed that these nonlinear effects influence the breakdown threshold only for NA < 0.9. Self-focusing and filamentation may play a role well above the breakdown threshold but are not relevant for the pulse energies used in nano-surgery on cells.

The time evolution of the electron density ρ_c in the conduction band under the influence of a laser pulse with Gaussian temporal shape was calculated using a rate equation of the generic form (Noack and Vogel, 1999)

$$d\rho_c / dt = \eta_{\mathrm{photo}} + \eta_{\mathrm{casc}} \, \rho_c - \eta_{\mathrm{diff}} \, \rho_c - \eta_{\mathrm{rec}} \, \rho_c^{\,2} . \tag{4}$$

The first term represents the production of free electrons mediated by the strong electric field in the laser focus (photoionization via multiphoton and tunneling ionization), the second term represents the contribution of cascade ionization, and the last two terms describe the losses through diffusion of electrons out of the focal volume, and recombination. The cascade ionization rate η_{casc} and the diffusion loss rate η_{diff} are proportional to the number of already produced free electrons, while the recombination rate η_{rec} is proportional to ρ_c^2, as it involves an interaction between two charged particles (an electron-hole pair). Even though diffusion and recombination do not play a significant role during femtosecond laser pulses, they were included to enable a comparison to plasma formation by nanosecond pulses. The explicit form of the individual terms in Eq. (4) has been described in detail by Vogel et al. (2005).

The temporal evolution of the electron density, $\rho(t)$, was calculated for laser pulses focused into pure water at a numerical aperture of NA = 1.3. At least one free "seed" electron produced by photoionization is required for the start of the cascade. Therefore, the term for cascade ionisation is only considered after there is at least a 50% probability of having this start electron in the focal volume. The focal volume was assumed to be ellipsoidal, as discussed further below in section 3.

2.3 Evolution of free-electron density and breakdown thresholds

The top row of Fig. 2 presents the evolution of the free-electron density ρ_c during the laser pulse at the optical breakdown threshold for 6-ns, 1064-nm pulses, and for 100-fs, 800-nm pulses. To facilitate a comparison between the different pulse durations, the time t is normalized with the respective laser pulse duration τ_L. The contribution of photoionization to the total free-electron density is plotted as a dotted line. The bottom row of Fig. 2 shows

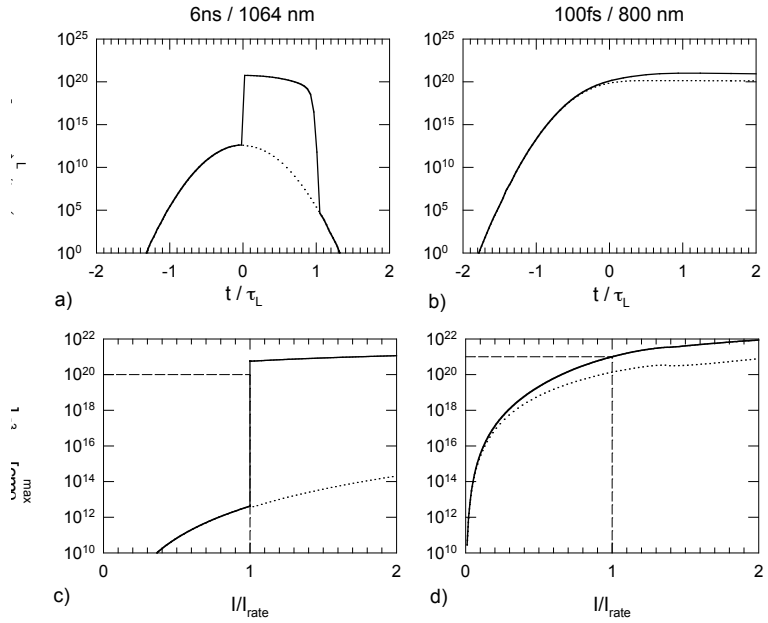

Figure 2. Top row: Evolution of the free-electron density during the laser pulse at the optical breakdown threshold for 6 ns, 1064 nm pulses and for 100 fs, 800 nm pulses. The time t is normalized with respect to the laser pulse duration τ_L. The contribution of multiphoton ionization to the total free-electron density is plotted as a dotted line. Bottom row: Maximum free electron density ρ_{max} achieved during the laser pulse as a function of irradiance, for the same laser parameters. The irradiance I is normalized with respect to the threshold irradiance I_{rate}. The threshold I_{rate} and the corresponding value of ρ_{max} are marked by dotted lines.

how the maximum free electron density achieved during the laser pulse depends on irradiance.

The dynamics of plasma formation is extremely different for nanosecond and femtosecond pulses. With nanosecond pulses, no free electrons are formed for irradiance values below the optical breakdown threshold because the irradiance is too low to provide seed electrons by means of multiphoton ionization (Fig 2c). Once the irradiance is high enough to provide a seed electron, the ionization cascade can start. It proceeds very rapidly owing to the high irradiance (Fig. 2a). The electron density shoots up by 9 orders of magnitude within a small fraction of the laser pulse duration until its rise is stopped by recombination which is proportional to ρ_c^2. The breakdown threshold is, hence, extremely sharp - either is a highly ionized plasma produced, or no plasma at all. These numerical predictions are supported by the experimental observation that at the threshold of nanosecond optical breakdown with IR laser pulses the transmission of the focal volume drops abruptly to less than 50% of the value without plasma formation (Nahen and Vogel, 1996, Noack, 1998c). The transmission loss for shorter pulse durations is much less abrupt (Nahen and Vogel. 1996, Noack et al., 1998b, Noack 1998c, Vogel et al., 1999).

With femtosecond pulses, a much higher irradiance is necessary for optical breakdown to be completed during the laser pulse duration than with nanosecond pulses. This favors the generation of free electrons through photoionization because multiphoton ionization exhibits a strong irradiance dependence $\propto I^k$ (k representing the number of photons required for crossing the ionization potential) as opposed to $\propto I$ for the cascade ionization rate (Vogel et al., 2005). While with nanosecond pulses the total number of free electrons generated through avalanche ionization is 10^9 times larger than the number generated through multiphoton ionization (Fig. 2a), it is only 12 times larger with 100-fs pulses at 800 nm (Fig. 2b). As a consequence of the increasing importance of multiphoton ionization with shorter pulse durations, there is never a lack of seed electrons for avalanche ionization. An avalanche is initiated at irradiance values considerably lower than the breakdown threshold. The free-electron density reached at the end of the avalanche depends on irradiance in a much smoother way (Fig. 2d) than for ns pulses (Fig. 2c). Therefore, one can generate any desired free-electron density by selecting an appropriate irradiance value.

Fig. 3 presents threshold values for irradiance, I_{rate}, and radiant exposure, $F_{rate} = I_{rate} \times \tau_L$, required to reach a critical free electron density of $\rho_{cr} = 10^{21}$ cm^{-3}. The thresholds were calculated for various wavelengths and pulse durations ranging from 10 fs to 10 ns. Two regimes can be distinguished: For $\tau_L < 10$ ps, the threshold radiant exposure F_{rate} exhibits only a weak dependence on pulse duration. This reflects the fact that recombination

plays only a minor role during ultrashort laser pulses. Therefore, only one set of free electrons is produced that corresponds to an approximately constant energy density within the focal volume. This is in accordance with the experimental threshold criterion of bubble formation that requires a specific energy density, which varies little with laser parameters. By contrast, for longer pulses more than one set of free electrons is produced and recombines during the laser pulse. Here it is the threshold irradiance I_{rate} that remains approximately constant, because a minimum irradiance is required to provide the seed electrons for the ionization cascade by multiphoton ionization and to drive the cascade sufficiently fast to reach the critical free electron density within the laser pulse duration. As a consequence, the radiant exposure threshold and plasma energy density increase steeply with increasing pulse duration.

The predicted form of the F_{rate} (τ_L) dependence qualitatively matches experimental observations on the pulse duration dependence of single shot damage thresholds at surfaces of transparent large-band-gap dielectrics (Du et

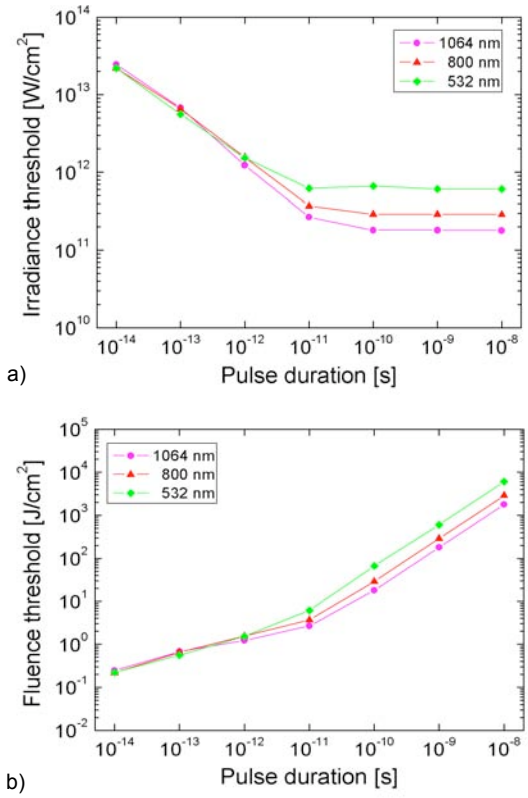

Figure 3. Calculated optical breakdown thresholds ($\rho_{cr} = 10^{21}$ cm^{-3}) as a function of laser pulse duration for various wavelengths; (a) irradiance threshold, (b) radiant exposure threshold.

al., 1996, Tien et al., 1999) and ablation thresholds of corneal tissue (Du et al., 1994).

2.4 Low-density plasmas in bulk media

Fig. 2d indicates that femtosecond pulses focused into bulk transparent media can create low-density plasmas in which the energy density remains below the level that leads to cavity formation in the medium. Experimental evidence for the existence of such low-density plasmas was provided by Mao et. al. (2004) through measurements of the free electron density in MgO and SiO_2. Free electrons are produced in a fairly large irradiance range below the optical breakdown threshold, with a deterministic relationship between free electron density and irradiance. Low-density plasmas thus offer the possibility to deliberately produce chemical changes, heating, and thermomechanical effects by varying the irradiance.

For larger irradiances, plasmas in bulk media grow beyond the region of the beam waist, which is not possible for plasma formation at surfaces. At surfaces, the energy deposition becomes confined to a thin layer of less than 100 nm thickness once the free electron density reaches the critical density because the superficial plasma layer is highly absorbing and reflecting (Stuart et al., 1996, von der Linde and Schüler, 1996, Joglekar et al., 2004, Feit et al., 2004). By contrast, in bulk media there is no restriction for the region of optical breakdown to spread towards the incoming laser beam with increasing irradiance. At large irradiances, breakdown starts to occur already before the femtosecond pulse reaches the beam waist, and both irradiance and beam propagation are influenced by the plasma generation (Hammer et al., 1997, Arnold et al., 2005). These effects shield the focal region, enlarge the size of the breakdown region, and limit the free electron density and energy density reached in the entire breakdown volume (Fan et al., 2002a, 2002b, Arnold et al., 2005, Rayner et al., 2005). Low density plasmas can, therefore, easily be produced in bulk media while at surfaces the self-induced confinement of plasma formation to a thin layer leads to a rapid rise of free electron density with irradiance, and the irradiance range in which low-density plasmas can be formed is very small (Stuart et al, 1996, Joglekar et al., 2004).

3 FOCAL IRRADIANCE- AND FREE-ELECTRON DISTRIBUTION

The temperature and stress distribution in the focal region depend on the distribution of quasi-free electrons produced during femtosecond optical breakdown. Therefore, we must explore the shape of the irradiance and free-

electron density distributions within the focal volume before we can investigate the resulting temperature and stress effects. The irradiance distribution in the focal volume of a diffraction limited microscope objective used to focus a plane wave has an approximately ellipsoidal shape (Born and Wolf, 1970, Ditlbacher et al., 2004, Vogel et al., 2005). For our numerical simulations, the focal volume will therefore be approximated by an ellipsoid with short axis d and long axis l. The short axis d of the ellipsoid is identified with the diameter of the central maximum of the Airy pattern in the focal plane

$$d = 1.22\,\lambda / NA\,. \tag{5}$$

The symbol λ refers to the vacuum wavelength of light. The refractive index of the medium is contained in the value of the numerical aperture (NA) of the microscope objective. The ratio l/d of the long and short axes is

$$l / d = (1 - \cos\alpha) / (3 - 2\cos\alpha - \cos 2\alpha)^{1/2} \tag{6}$$

for optical setups with very large solid angles (Grill and Stelzer, 1999). Here α is the half angle of the light cone such as used in the definition of the numerical aperture $NA = n_0 \sin\alpha$. For NA = 1.3, which in water corresponds to an angle of $\alpha = 77.8°$, we find $l/d = 2.4$. For $\lambda = 800$ nm, the above considerations yield focal dimensions of $d = 750$ nm, and $l = 1800$ nm.

The mathematical form of the diffraction-limited irradiance distribution in the Fraunhofer diffraction pattern of a microscope objective (Born and Wolf, 1970) is too complex for convenient computation of the temperature and stress evolution induced by optical breakdown. We approximate the ellipsoidal region of high irradiance in the center of the focal region by a Gaussian function

$$\rho_{\max}(r,z) = \rho_{\max}[I(0,0)] \exp[-2\,(r^2 / a^2 + z^2 / b^2)]\,. \tag{7}$$

where r and z are the coordinates in radial and axial direction, respectively, and $a = d/2$ and $b = l/2$ denote the short and long axis of the ellipsoid. The boundaries of the ellipsoid correspond to the $1/e^2$ values of the Gaussian irradiance distribution.

To derive the free-electron distribution $\rho_{\max}(r,z)$ from the irradiance distribution $I(r,z)$, we assume that for femtosecond pulses the free-electron density at the end of the laser pulse is approximately proportional to i^k, where k is the number of photons required for multiphoton ionization. This simplifying assumption corresponds to the low-intensity approximation of the Keldysh theory and neglects the weaker irradiance dependence of avalanche ionization

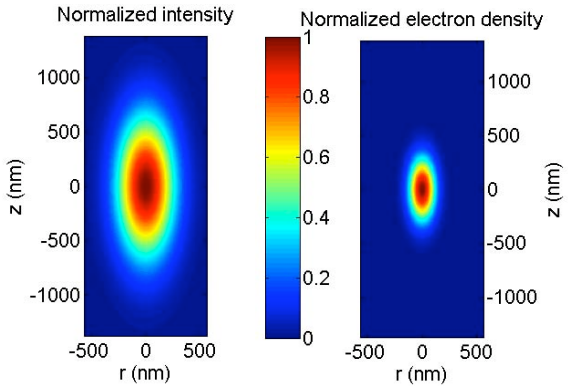

Figure 4. Normalized irradiance distribution (a) and electron density distribution (b) in the focal region for NA = 1.3 and λ = 800 nm that are assumed for the numerical calculations of the temperature and stress evolution induced by femtosecond optical breakdown.

that usually dominates plasma formation during the second half of a laser pulse (Fig. 2b). For $\rho_{max} \leq 5\times10^{20}$ cm^{-3}, the proportionality $\rho_{max} \propto I^k$ has been confirmed by the experimental results of M
ao et. al. (2004). The spatial distribution of the free-electron density can thus be expressed as

$$\rho_{max}(r,z) = \rho_{max}[I(0,0)] \exp[-2k\,(r^2/a^2 + z^2/b^2)] \ . \qquad (8)$$

Fig. 4 shows the irradiance and electron density distribution in the focal region according to Eqs. (7) and (8) for NA = 1.3 and λ = 800 nm, for which $k = 5$. Due to the nonlinear absorption process underlying optical breakdown, the free-electron distribution is much narrower than the irradiance distribution. For λ = 800 nm and breakdown in water, it is narrower by a factor of $\sqrt{5} = 2.24$, which corresponds to a reduction of the affected volume by a factor of 11.2 below the diffraction limited focal volume. The diameter of the free - electron distribution at the $1/e^2$- values amounts to 336 nm, the length to 806 nm. Femtosecond-laser nanoprocessing can achieve a 2-3 fold better precision than cell surgery using cw irradiation[5], and enables manipulation at arbitrary locations.

4. CHEMICAL EFFECTS

Plasma-mediated chemical effects of low-density plasmas in biological media can be classified into two groups: 1. Changes of the water molecules by which reactive oxygen species (ROS) are created that affect organic

molecules, 2. Direct changes of the organic molecules in resonant electron-molecule scattering.

1. The creation of ROS such as OH* and H_2O_2 through various pathways following ionization and dissociation of water molecules has been investigated by Nikogosyan et. al. (1983) and recently reviewed by Garret et al. (2005). Both oxygen species are known to cause cell damage (Tirlapur et al., 2001). Heisterkamp et. al. (2002) confirmed the dissociation of water molecules during femtosecond laser-induced plasma formation by chemical analysis of the gas content of the bubbles.

2. Capture of electrons into an antibonding molecular orbital can initiate fragmentation of biomolecules (Boudaiffa et al., 2000, Hotop, 2001, Gohlke and Illenberger, 2002, Huels et al., 2003, Garret et al., 2005). Such capture can occur when the electron possesses a "resonant" energy for which there is sufficient overlap between the nuclear wave functions of the initial ground state and the final anion state. For a molecule XY this process corresponds to $e^- + XY \rightarrow XY^{*-}$, where the XY^{*-} has a repulsive potential along the X-Y bond coordinate. After a time of 10^{-15} to 10^{-11} s, the transient molecular anion state decays either by electron autodetachment leaving a vibrationally excited molecule (VE), or by dissociation along one, or several specific bonds such as $XY^{*-} \rightarrow X^{\bullet} + Y^-$ (DA). Various authors describe resonant formation of DNA strand breaking induced by low-energy electrons (3-20 eV) (Boudaiffa et al., 2000, Gohlke and Illenberger, 2002, Huels et al., 2003). Boudaiffa et. al. (2000) found that the maximum single-strand break (SSB) and double-strand break (DSB) yields per incident electron are roughly one or two orders of magnitude larger than those for 10-25 eV photons. It is conceivable that accumulative effects of this kind can lead to a dissociation/dissection of biological structures that are exposed to femtosecond-laser-generated low-density plasmas.

The irradiance threshold for chemical changes by low-density plasmas can be assessed using the plot of free-electron density versus irradiance presented in Fig. 2d. At NA = 1.3 and 800 nm wavelength, one free electron per focal volume corresponds to a density of $\rho = 2.1\times10^{13}$ cm^{-3}. Our calculations yield the result that this value is reached at an irradiance of $I = 0.26\times10^{12}$ W cm^{-2} which is 0.04 times the irradiance threshold for breakdown defined as $\rho_c = \rho_{cr} = 10^{21}$ cm^{-3}. Tirlapur et. al. (2001) experimentally observed membrane dysfunction and DNA strand breaks leading to apoptosis-like cell death after scanning irradiation of PtK2 cells with a peak irradiance of $I \approx 0.44\times10^{12}$ W/cm^{-2} in the focal region, or 0.067 times the calculated breakdown threshold. The observed damage pattern of membrane dysfunction and DNA strand breaks matched the effects expected from ROS and free electrons. The damage resembled the type of injury otherwise associated with single photon aborption of UV radiation (Tirlapur et al., 2001). However, in Tirlapur's

experiments it arose through nonlinear absorption of NIR irradiation and the exposure of cells to low-density plasmas.

The irradiance producing lethal changes when laser pulse series are scanned over entire cells ($0.067 \times I_{rate}$) is slightly higher than the model prediction for the irradiance producing one free electron per pulse in the focal volume ($0.04 \times I_{rate}$). According to our model, about 10 free electrons in the focal volume are produced by each laser pulse when lethal changes occur. Considering that the cell is exposed to thousands of pulses during the scanning irradiation, cumulative chemical damage may easily arise from the free electrons. By contrast, when locally confined irradiation is used to achieve knockout of individual cell organelles or intracellular dissection, the irradiance threshold for cell death is considerably higher, and dissection can be performed without affecting cell viability.

5. TEMPERATURE EVOLUTION

5.1 Calculation of temperature distribution

The deposition of laser energy into the medium is mediated by the generation and subsequent acceleration of free electrons. The energy carried by the free electrons is transferred to the heavy particles in the interaction volume through collisions, electron hydration, and nonradiative recombination processes resulting in a heating of the atomic, molecular and ionic plasma constituents. To assess the time needed to establish an equilibrium temperature, we need to look at the characteristic time for electron cooling (the transfer of kinetic electron energy during collisions) and at the time scale for recombination which in water progresses through hydration of the free electrons. The time constant for electron cooling is in the order of only a few picoseconds (Nolte et al., 1997), and the time constant for hydration of free electrons in water is even shorter, about 300 fs (Nikogosyan et al., 1983). However, the hydrated states possess a relatively long life time of up to 300 ns (Nikogosyan et al., 1983). In the framework of our model, the different steps are treated as one recombination process. As the frequency of recombination events is proportional to ρ_c^2, the recombination time depends on the free-electron density. It takes about 40 ps until the free electron density decreases by one order of magnitude from a peak value of $\rho_c = 10^{20}$ cm^{-3}, and about 20 ps for a peak value of $\rho_c = 10^{21}$ cm^{-3} (Noack and Vogel, 1999, Vogel and Noack, 2001). For low-density plasmas it will thus take between a few picoseconds and tens of picoseconds until a "thermodynamic" temperature is established (Garret et al., 2005).

The temperature rise can be determined by calculating the volumetric energy density gained by the plasma during the laser pulse. This calculation is particularly easy for femtosecond pulses because the pulse duration is considerably shorter than the electron cooling and recombination times. Therefore, hardly any energy is transferred during the laser pulse, and the energy density deposited into the interaction volume is simply given by the total number density ρ_{max} of the free electrons produced during the pulse multiplied by the mean energy gain of each electron. The mean energy gain of an electron is given by the sum of ionization potential $\widetilde{\Delta}$ and average kinetic energy, the latter of which is $(5/4)\widetilde{\Delta}$ for free electrons produced by cascade ionization (see section 2 and Fig. 1). This yields the following simple relation for the plasma energy density ε at the end of the laser pulse:

$$\varepsilon = \rho_{max}\,(9/4)\,\widetilde{\Delta} \tag{9}$$

The temperature rise in the interaction volume after a single laser pulse can then be calculated by $\Delta T = \varepsilon / (\rho_0 C_p)$, where C_p is the heat capacity and ρ_0 the mass density of the medium. The evolution of the temperature distribution after single 100-fs pulse (λ = 800 nm) during application of series of 100-fs pulses emitted at various repetition rates was calculated by solving the differential equation for heat diffusion as described by Vogel et al. (2005).

5.2 Evolution of the temperature distribution

The spatial temperature distribution at the end of a single fs-laser pulse, before heat diffusion sets in, reproduces the shape of the free-electron distribution of Fig. 4. Hence, the diameter of the initial temperature distribution ($1/e^2$- values) amounts to 336 nm, the length to 806 nm. Fig. 5 shows the calculated temperature evolution at the center of the laser focus when series of 800-nm, 100-fs pulses are focused into water at different repetition rates (80 MHz and 1 MHz) and numerical apertures (NA = 1.3 and NA = 0.6). It was assumed that with each pulse an energy density of 1 J cm^{-3} at the center of the initial temperature distribution is deposited. For other values of the volumetric energy density, the shape of the temperature vs time curve will be the same but the absolute values of the temperature varies proportional to the peak density of absorbed power. For comparison, we also calculated the temperature evolutions during cw irradiation with the same average power as for the pulsed irradiation. For 80 MHz repetition rate, pulsed and continuous energy deposition differ significantly only during the first 100 ns.

The calculations in Fig. 5a for tightly focused irradiation with 80 MHz repetition rate reveal that the temperature is only 6.8 times larger after a few

microseconds than the temperature increase caused by a single pulse. This implies that only a moderate heat accumulation occurs during plasma-mediated cell surgery. However, when the numerical aperture is reduced from NA = 1.3 to NA = 0.6, such as in Fig. 5b, a 45-fold temperature increase is predicted. Temperature accumulation can almost entirely be avoided if, at the same NA, the repetition rate is lowered to 1 MHz (Fig. 5c). In this case, the

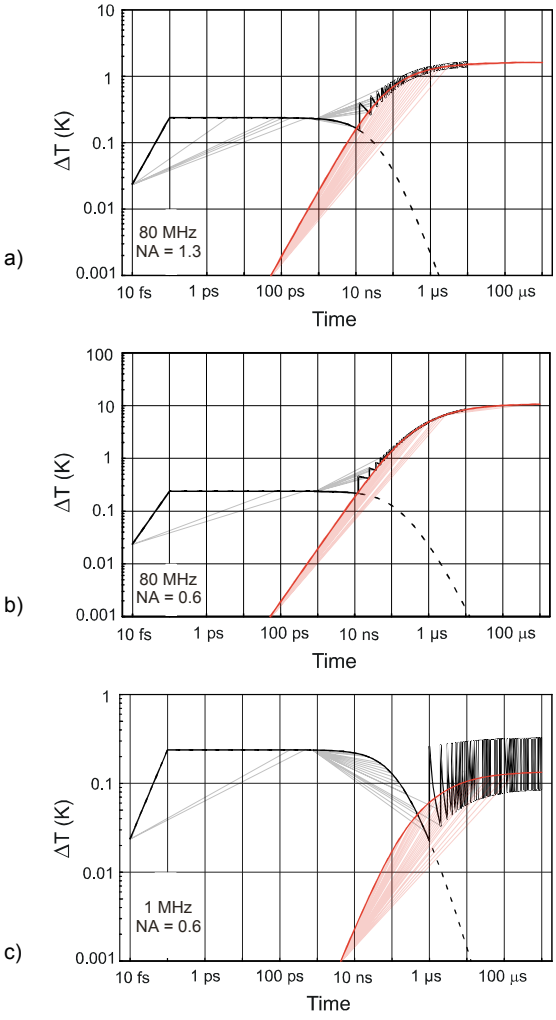

Figure 5. Temperature evolution at the center of the laser focus produced by a series of 800 nm, 100 fs pulses focused into water. a) 80 MHz repetition rate, NA = 1.3; b) 80 MHz repetition rate, NA = 0.6; c) 1 MHz repetition rate, NA = 0.6. The volumetric energy density deposited per pulse is always 1 Jcm^{-3}at the focus center. The dashed lines represent the temperature decay after a single pulse. For comparison, the temperature evolution during cw irradiation with the same average power as for the pulsed irradiation is also shown.

peak temperature in a long pulse series is only 1.36 times larger than after a single pulse. For 1 MHz repetition rate and NA = 1.3, this factor reduces to 1.024.

When laser surgery is performed with 80 MHz pulse series focused at NA = 1.3, the boiling temperature of 100°C will, due to the 6.8-fold temperature accumulation, be reached when each individual pulse produces a temperature rise of 11.8°C (starting from 20°C room temperature). For 800-nm, 100-fs pulses this temperature rise requires a free-electron density of $\rho_c = 2.1\times10^{19}$ cm^{-3}, which is reached at an irradiance of 0.51 times the value required for optical breakdown ($\rho_{cr} = 10^{21}$ cm^{-3}).

The evolution of the temperature distribution in the vicinity of the focus during application of 80-MHz pulse series is presented in Fig. 6 for NA = 1.3. The temperature distribution remains fairly narrow (FWHM ≈ 600 nm in radial direction) even after a few milliseconds when a dynamic equilibrium between energy deposition and heat diffusion has been established. This is related to the small size of the focal volume which allows for rapid heat diffusion in all directions. For NA = 0.6, the temperature distribution is significantly broader (radial FWHM ≈ 1.5 µm, axial FWHM ≈ 2.900 µm).

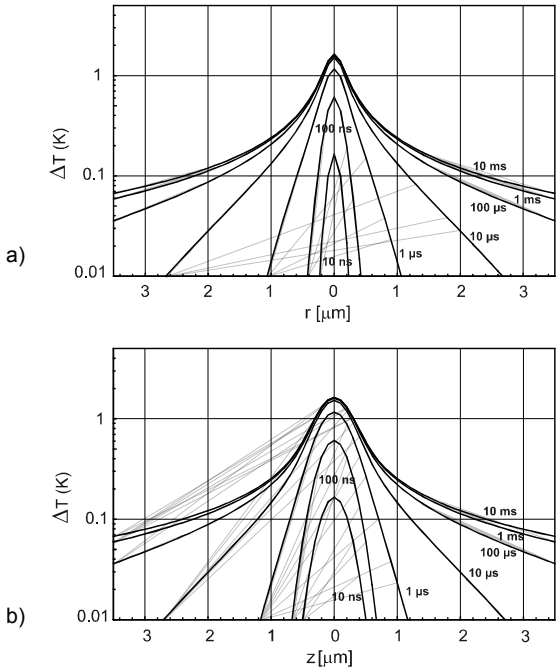

Figure 6. Temperature distribution in radial direction and axial direction produced by series of 800-nm, 100-fs pulses focused into water at numerical apertures of NA = 1.3 at a pulse repetition rate of 80 MHz. The volumetric energy density deposited at the focus center was 1 J cm^{-3} for each pulse.

At first sight, the results of our temperature calculations might suggest that an irradiance range below the optical breakdown threshold exists where predominantly thermal effects in biological media can be produced. However, one needs to consider that about 10^6 free electrons per pulse are generated in the focal volume at the irradiance which creates a temperature difference of 11.8°C per pulse and a peak temperature of 100°C after a pulse series of several microseconds (for NA = 1.3). Any thermal denaturation of biomolecules will thus always be mixed with free-electron-induced chemical effects, and the latter will probably dominate.

6 THERMOELASTIC STRESS GENERATION AND STRESS-INDUCED BUBBLE FORMATION

6.1 Calculation of stress distribution and bubble formation

The temperature rise in the focal volume occurs during thermalization of the energy carried by the free electrons, i. e. within a few picoseconds to tens of picoseconds (see section 5.1). This time interval is much shorter than the acoustic transit time from the center of the focus to its periphery. Therefore, no acoustic relaxation is possible during the thermalization time, and the thermoelastic stresses caused by the temperature rise stay confined in the focal volume, leading to a maximum pressure rise (Paltauf and Schmidt-Kloiber, 1999, Paltauf and Dyer, 2003, Vogel and Venugopalan, 2003). Conservation of momentum requires that the stress wave emitted from a finite volume within an extended medium must contain both compressive and tensile components such that the integral of the stress over time vanishes (Sigrist and Kneubühl, 1978, Paltauf and Schmidt-Kloiber, 1999). In water, the tensile stress will cause the formation of a cavitation bubble when the strength of the liquid is exceeded. For cell surgery, the threshold for bubble formation defines the onset of disruptive mechanisms contributing to dissection.

To determine the evolution of the thermoelastic stress distribution in the vicinity of the laser focus, we solved the three-dimensional thermoelastic wave equation. A starting point for the calculation of the thermoelastic stress wave propagation is the temperature distribution at the end of a single femtosecond laser pulse, which reproduces the free-electron distribution described by Eq. (8). In the following calculations, this temperature distribution is characterized by T_{max}, the temperature in °C in the center of the focal volume. From this temperature distribution, the initial thermoelastic pressure before the acoustic wave has started to propagate was calculated using

$$p(\vec{r}) = \int_{T_1}^{T_2(\vec{r})} \frac{\beta(T)}{\hat{E}(T)} dT, \tag{10}$$

where T_1 = 20°C is the temperature before the laser pulse, and $T_2(\vec{r})$ the temperature of the plasma after the laser pulse, which depends on the location within the focal volume. The temperature dependence of the thermal expansion coefficient β and the compressibility K was taken into account, using values for metastable water reported by Skripov et al. (1988). The time- and space-dependent pressure distribution $p(\vec{r},t)$ due to the relaxation of the initial thermoelastic pressure was calculated using a *k*-space (spatial frequency) domain propagation model Köstli et al., 2001, Cox and Beard, 2005).
Because the heated volume is very small (≈0.07 μm^3) and the region subjected to large tensile stress amplitudes is even smaller (see Fig. 14, below), the presence of inhomogeneous nuclei that could facilitate bubble formation is unlikely. Therefore, we have to consider the tensile strength of pure water to estimate the bubble formation threshold in femtosecond optical breakdown. We use the crossing of the "kinetic spinodal" as defined by Kiselev (1999) as threshold criterion for bubble formation. In the thermodynamic theory of phase transitions, the locus of states of infinite compressibility $(\delta p / \delta V)_T = 0$, the spinodal, is considered as a boundary of fluid metastable (superheated) states. Physically, however, the metastable state becomes short-lived due to statistical fluctuations well before the spinodal is reached (Skripov et al., 1988, Debenedetti, 1996). The "kinetic spinodal" is the locus in the phase diagram where the lifetime of metastable states becomes shorter than a relaxation time to local equilibrium. If the surface tension is known, the physical boundary of metastable states in this approach is completely determined by the equation of state only, i.e. by the equilibrium properties of the system (Kiselev, 1999).

In Fig. 7, the kinetic spinodal is plotted together with the peak compressive and tensile thermoelastic stresses in the focus center that are produced when an 800-nm, 100-fs pulse is focused into water at NA = 1.3. The temperature at which the tensile stress curve reaches the kinetic spinodal is defined as bubble formation threshold. For larger laser pulse energies, the kinetic spinodal will be reached in an increasingly large part of the focal region.

To calculate the dynamics of the cavitation bubble produced after crossing the kinetic spinodal, first the size of the bubble nucleus was determined. It was identified with the extent of the region in which the negative pressure exceeds the kinetic spinodal limit $p(\vec{r},t) < p_{ks}(\vec{r})$. The initial radius of a spherical bubble with the same volume was taken as the starting nucleus for the cavitation bubble. The heated and stretched material within the nucleus commences to expand instantaneously (within less than 1 ps) once the kinetic

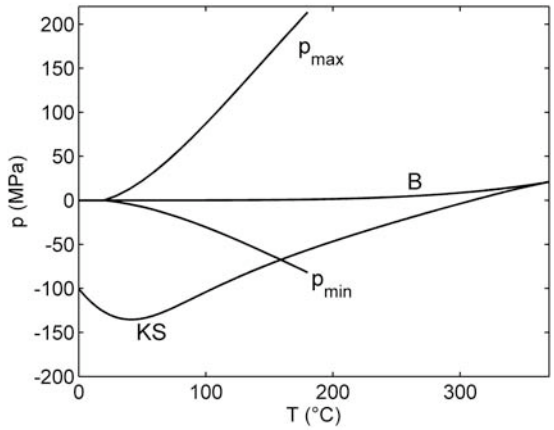

Figure 7. Peak compressive and tensile thermoelastic stresses in the focus center produced by a 800-nm, 100-fs pulse focused into water at NA = 1.3, plotted as a function of temperature together with the binodal (B) and the kinetic spinodal (KS) of water. The kinetic spinodal was calculated by Kiselev (1999) using the analytic equation of state of Saul and Wagner (1989).

spinodal is reached (Garrison et al, 2003). As driving force for the expansion only the negative part of the time-dependent stress in the center of the focal volume was considered, because the nucleus does not exist before the tensile stress arrives.

After the passage of the tensile stress transient, the vapor pressure p_v inside the bubble continues to drive the bubble expansion. The initial vapor pressure is calculated for a temperature averaged over all volume elements within the nucleus. During bubble growth, it will drop due to the cooling of the expanding bubble content. This cooling is counteracted by heat diffusion into the bubble from the liquid surrounding the bubble. The temperature of this liquid, on the other hand, drops because of heat diffusion out of the focal volume. To quantify the temporal evolution of the driving pressure, we consider two limiting cases defined by (1) isothermal, and (2) adiabatic conditions for the bubble content with respect to the surrounding liquid (Vogel et al., 2005). In case 2, the vapor pressure in the bubble drops considerably faster than in case 1. In both cases, the ongoing phase transition in the bubble was neglected to obtain tractable expressions for $p_v(t)$. This simplification enabled us to use the Gilmore model to describe the cavitation bubble dynamics (Gilmore, 1952, Knapp et al., 1971, Paltauf and Schmidt-Kloiber, 1996). To obtain a correct description of the buble dynamics in a heated and stretched liquid, we considered the temperature-dependence of the surface tension at the bubble wall (NIST, 2005). This is a refinement of our previous study (Vogel et al., 2005) in which we assumed a constant value (surface tension at room temperature) in all calculations.

6.2 Evolution of the stress distribution

The thermalization time of the energy carried by the free electrons was assumed to be 10 ps. For NA = 1.3, and λ = 800 nm, and a sound velocity in water of c_0 = 1500 m/s, the acoustic transit time to the periphery of the heated region with 168 nm radius is 112 ps. Thus the dimensionless thermalization time (thermalization time divided by acoustic relaxation time) is $t_p^* = 0.09$, which corresponds to a very high degree of stress confinement. The "thermalization pulse" used to calculate the temperature and pressure rise by means of Eq. (10) was assumed to have a Gaussian temporal shape, with peak at $t = 0$.

Fig. 8 shows the spatial stress distribution in radial and axial direction for various points in time after the release of the laser pulse, normalized to the

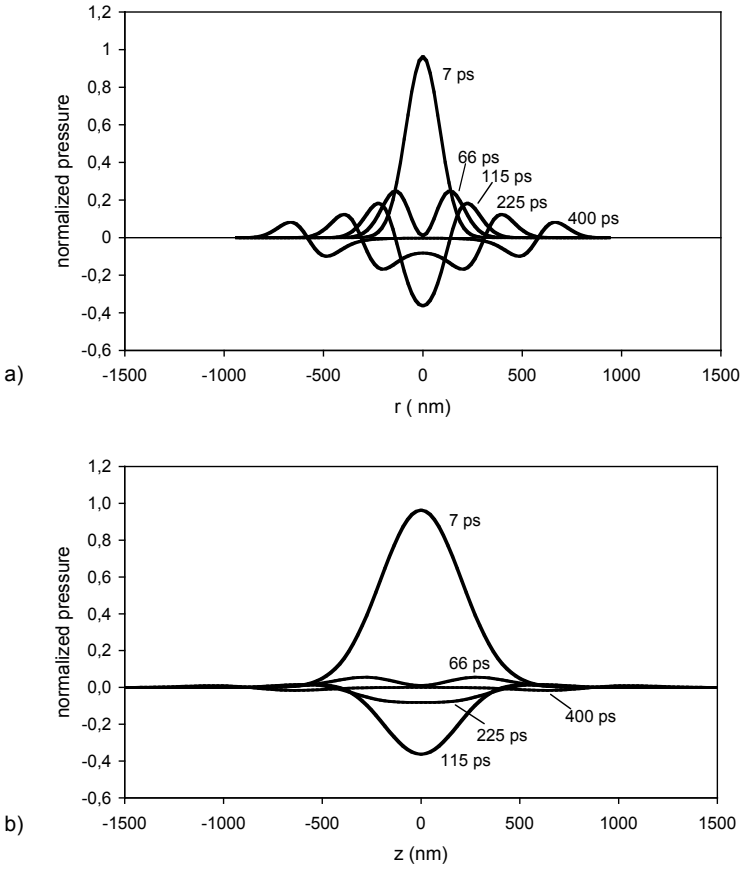

Figure 8. Stress distribution produced by a single femtosecond pulse of 800 nm wavelength focused into water (NA = 1.3), for various times after the release of the laser pulse; (a) in radial direction, (b) in axial direction. The pressure amplitudes are normalized to the peak compressive stress created in the focal volume.

peak compressive stress. The compressive stress generates a stress wave traveling into the surrounding medium. When the thermal expansion comes to a rest, inertial forces lead to the generation of a relaxation wave that propa gates from the periphery of the focal volume towards its center and is focused in the center of symmetry. Because of the geometrical focusing, it turns into atensile stress wave that achieves maximum amplitude at the center of symmetry. The duration of the entire stress wave is ≈ 200 ps. The stress wave amplitudes outside the focal region have a bipolar shape as expected for thermoelastic waves. Because of the elongated shape of the focal volume, they are considerably larger in radial than in axial direction.

Measurements of the stress waves produced by femtosecond optical breakdown at large NA and close to the breakdown threshold are very challenging because of the sub-micrometer size of the breakdown volume and the sub-nanosecond duration of the stress transients. Therefore, we performed measurements at smaller numerical aperture (NA = 0.2) to assess the stress amplitudes arising during femtosecond optical breakdown. Investigations for irradiances well times above the breakdown threshold were done by means of streak photography and subsequent digital image analysis of the streak recordings (Noack and Vogel, 1998a, Noack et al., 1998b). Differentiation of the stress wave propagation curves $r(t)$ obtained from the streak recordings yields the stress wave velocity that is related to the pressure amplitude by the known Rankine-Hugoniot-relationship for water (Rice and Walsh, 1957). The analysis provides the entire pressure vs distance curve perpendicular to the optical axis in the vicinity of the breakdown region as shown in Fig. 9.

The determination of the shock wave pressure becomes inaccurate for pressure amplitudes below 100 MPa where the deviation of the propagation velocity from the sonic velocity becomes too small to be measured accurately with the streak technique (Noack and Vogel, 1998a). Therefore, the streak technique could only be applied for shock wave measurements at energies 15-150 times above the breakdown threshold. Stress wave amplitudes closer to the optical breakdown threshold were determined indirectly by hydrophone measurements at 6 mm distance from the focus (Noack, 1998c) and extrapolation of these data to the plasma rim. Measurement results for energies from close to the breakdown threshold up to 80 times threshold are shown in Fig. 10.

The results of far-field hydrophone measurements can be extrapolated to the boundary of the focal region if the decay constant n of the pressure decay $p \propto r^n$ with increasing propagation distance r is known. The decay constant was determined to n = 1.13 by comparing pressure values at the plasma rim and in the far-field that were measured at larger laser pulse energies. From the data in Fig. 10 a pressure of ≈0.008 MPa at 6 mm distance is deduced for the threshold energy $E = E_{th}$. This corresponds to a pressure value of 61 MPa

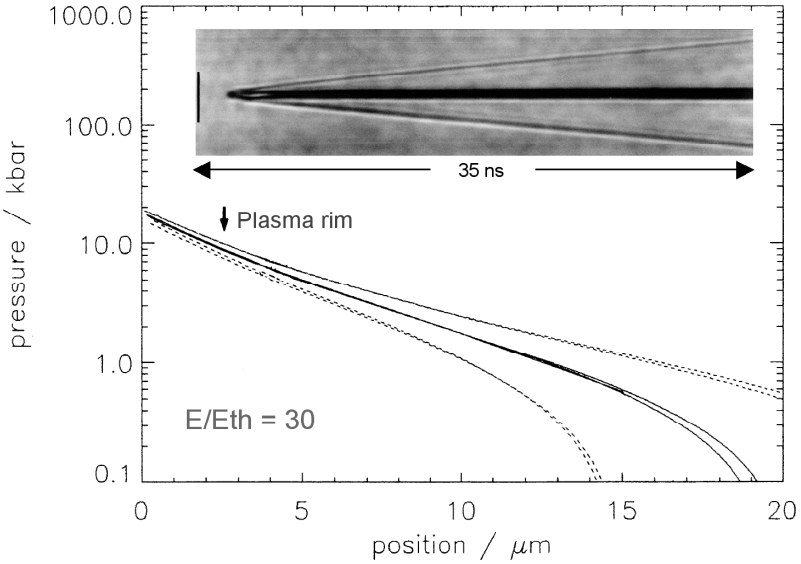

Figure 9. Measured pressure vs propagation distance curve for a stress wave produced by a 100-fs, 580-nm pulse of 5 μJ energy (E/E_{th} = 30) focused into distilled water at NA = 0.2 (16° full focusing angle). The arrow represents the location of the plasma rim as determined from plasma photographs in side view. The $p(d)$ curve was determined from the streak recording of the stress wave emission shown in the insert.

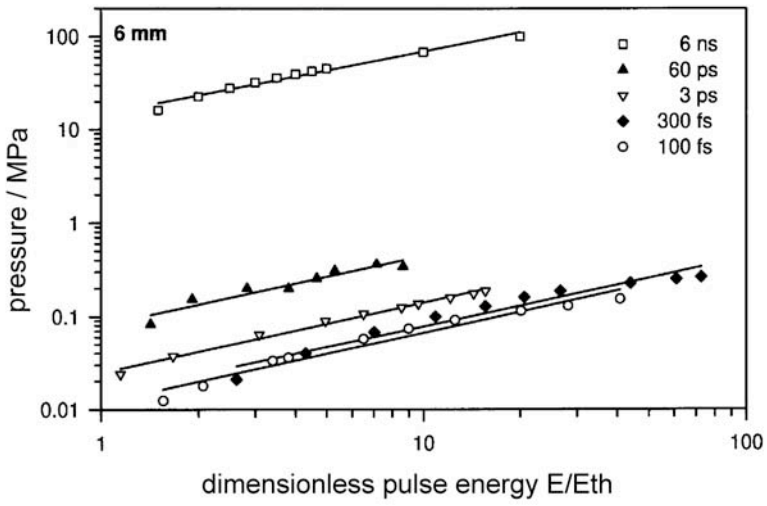

Figure 10. Stress wave amplitude for 100-fs pulses and longer pulse durations as a function of the dimensionless laser pulse energy E/E_{th}. The pressure amplitudes were measured by means of a hydrophone at 6 mm distance from the laser focus. Extrapolation of the data for 100-fs pulses to $E/E_{th} = 1$ yields a pressure value of ≈ 0.008 MPa.

at the plasma rim when a decay constant n = 1.13 is assumed. The plasma radius at E_{th} is identified with the focal radius of 2.2 μm that was measured using a knife edge technique (Noack, 1998c).

Our calculations of the thermoelastic stress generation predict a peak pressure of 181 MPa at the bubble formation threshold (see section 6.3 below). According to Fig. 8a, the stress transient that leaves the heated region in radial direction has a peak pressure of ≈25% of the maximum compressive amplitude within the focal volume. We thus obtain a theoretical prediction of 45 MPa for the amplitude of the thermoelastic stress wave at the plasma rim. Considering the uncertainties in the location of the plasma rim and the differences in numerical aperture between experiment and calculation, the agreement between experimental results (61 MPa) and calculated data (45 MPa) is very good.

Both experiments and calculations reveal that stress confinement in femtosecond optical breakdown results in the generation of high pressure values even though the temperature rise is only relatively small. In a purely thermal process starting from room temperature, a temperature rise of, for example 180°C would produce a saturation vapor pressure of 1.6 MPa. The compressive pressure transient produced by the same temperature rise under stress confinement conditions has an amplitude of 220 MPa which is more than two orders of magnitude larger than the vapor pressure.

The situation is different for optical breakdown at longer pulse durations where the stress confinement condition is not fulfilled. Here, high pressures are always associated with high temperatures and plasma energy densities. For pulses longer than the thermalization time of the free-electron energy, a dynamic equilibrium between generation of free electrons and thermalization of their energy is established during the laser pulse (Noack and Vogel, 1999). This leads to high value of the plasma energy density in the order of 30-40 $kJcm^{-3}$ for ns-pulses Vogel et al., 1996b, Vogel et al., 1999) and temperatures of several thousand degrees Kelvin (Stolarski et al., 1995). The duration of the resulting shock wave is determined by the time it takes for the high pressure within the plasma to decrease during the plasma expansion (Vogel et al., 1996b). For NA = 0.9, it was found to be about 25-40 ns (Venugopalan et al., 2002). By contrast, the duration of the thermoelastic stress transients is determined by the geometric dimensions of the breakdown volume which are in the sub-micrometer range. This leads to a duration of the stress transients of less than 300 ps.

6.3 Threshold for stress-induced bubble formation

The tensile stress produced during femtosecond optical breakdown makes it possible that a cavitation bubble can be generated by a relatively small tem-

perature rise in the liquid. The threshold for bubble formation is defined by the temperature rise leading to a crossing of the kinetic spinodal, as shown in Fig. 7. For λ = 800 nm, NA = 1.3, and a room temperature of 20°C, the critical temperature rise and the corresponding critical tensile stress are ΔT = 139°C, and p = -67.5 MPa, respectively. The corresponding compressive pressure is 181 MPa.

The temperature rise of 139°C at the threshold for bubble formation corresponds to an increase in energy density of 582 J cm^{-3} which, according to Eq. (9), is produced by a free-electron density of $\rho_c = 0.249\times10^{21}$ cm^{-3}. This electron density is less than the breakdown criterion of $\rho_{cr} = 10^{21}$ cm^{-3} assumed in our numerical calculations and in most other theoretical studies of plasma formation. The discrepancy between the threshold values relying on different breakdown criteria needs to be kept in mind when comparing the results of experimental studies, where bubble formation serves as breakdown criterion, with those of numerical simulations.

The fact that femtosecond optical breakdown is associated with only a relatively small temperature rise explains why plasma luminescence is no longer visible for pulse durations shorter than about 10 ps (Kennedy et al., 1997, Noack et al., 1998b). For pulse durations longer than the thermalization time, large amounts of energy are transferred from the free electrons to the heavy particles during the laser pulse (Noack and Vogel, 1999), resulting in a temperature of several thousand degrees Kelvin, bubble formation, and a bright plasma luminescence (Barnes and Rieckhoff, 1968, Stolarski et al., 1995, Chapyak et al., 1997). By contrast, a peak temperature of 159°C reached at the threshold for bubble formation with 100-fs pulses is too low to produce blackbody radiation in the visible range of the optical spectrum. Moreover, the recombination radiation of femtosecond-laser-produced plasmas is weak because only one "set" of free electrons is produced that recombines after the end of the laser pulse. Therefore, bubble formation is a more practical breakdown criterion for ultra-short laser pulses than plasma luminescence.

A comparison between experimental threshold data from various researchers and threshold values predicted by our model (Fig. 3) has been compiled by Vogel et al. (2005). Our numerical predictions lie within the range of experimental data for all pulse durations. However, the experimental data scatter within a range of one order of magnitude for femtosecond and nanosecond pulses, and only slightly less for picosecond pulses. These large variations reflect the difficulty of performing precise threshold measurements in the bulk of water. The measurements were influenced either by aberrations in the focusing optics, mode beating of longitudinal resonator modes resulting in picosecond intensity peaks during nanosecond pulses, or nonlinear beam propagation. A numerical aperture NA $\geq$ 0.9 is required for a pulse duration of 100 fs exclude a diminution of the spot size by self-focusing and the

corresponding apparent reduction of the breakdown threshold (Schaffer et al., 2001). Future measurements with aberration-free temporally Gaussian laser pulses focused at large NA will have to provide a reliable data base.

In addition, a better adjustment of the numerical breakdown criterion to the experimental criterion of bubble formation is needed to enable a meaningful comparison of experimental data with model predictions. While bubble formation requires an approximately constant energy density within the focal volume for all laser pulse durations and wavelengths, the energy density associated with a fixed value of the free electron density, such as $\rho_{cr} = 10^{21}$ cm^{-3}, varies considerably with pulse duration. Thus the assumption of a constant free electron density as breakdown criterion is quite arbitrary, especially for cases where the threshold is smooth, i.e. where ρ_{max} increases continuously with irradiance. In these cases it seems more reasonable to relate the critical free electron density to the energy density within the medium that leads to bubble formation. Equation (9) provides the required link between electron and energy density, and an analysis of ρ_{max} (I/I_{rate}) curves such as in Fig. 2 then yields the corresponding threshold irradiance.

6.4 Cavitation bubble dynamics

Fig. 11 shows a 2-D representation of the evolution of the thermoelastic stress wave and of the region in which the kinetic spinodal is surpassed (bubble nucleus) for a peak temperature of 200°C, slightly above the threshold for bubble formation. The subsequent bubble dynamics is shown in Fig. 12, and the dependence between maximum bubble radius and peak temperature is presented in Fig. 13. We see that very similar bubble sizes are predicted for cases 1 and 2, respectively (isothermal and adiabatic conditions for the bubble content with respect to the surrounding liquid). Moreover, the bubble motion in case 2 (adiabatic conditions) is almost identical to that in a third case where the vapor pressure is not at all taken into account and only the negative pressure pulse drives the bubble expansion (not shown). This implies that the thermoelastic stress is more important for driving the bubble expansion than the vapor pressure.

The most prominent feature of the transient bubbles produced close to the threshold of femtosecond optical breakdown is their small size and short lifetime. The bubble radius amounts to only about 200 nm in water, and will be even smaller in a visco-elastic medium such as the cytoplasm. This makes a dissection mechanism associated with bubble formation compatible with intracellular nanosurgery, in contrast to nanosecond optical breakdown (6 ns, 1064 nm) where the smallest bubble radius in water observed detected for NA = 0.9 was $R_{max} = 45$ µm (Venugopalan et al., 2002). The small bubble size corresponds to a small energy

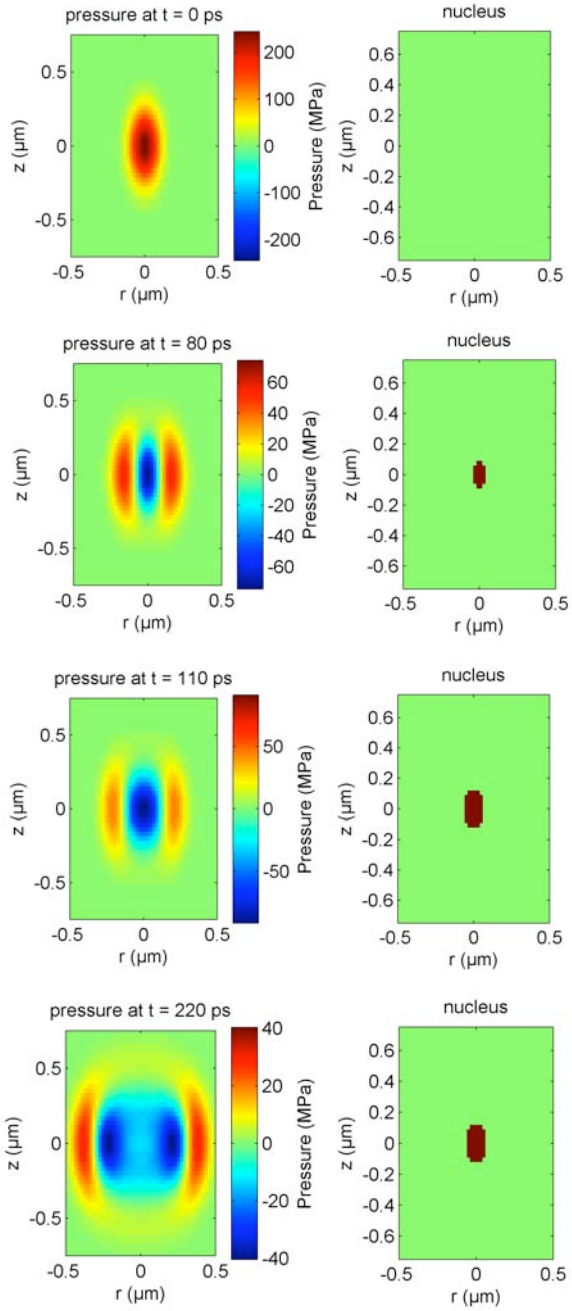

Figure 11. 2-D Plots of thermoelastic stress evolution (left), and of the region in which the kinetic spinodal limit is exceeded (right). This region demarcates the size of the bubble nucleus that is then expanded by the thermoelastic tensile stress wave. The calculations were performed for a peak temperature of 200°C.

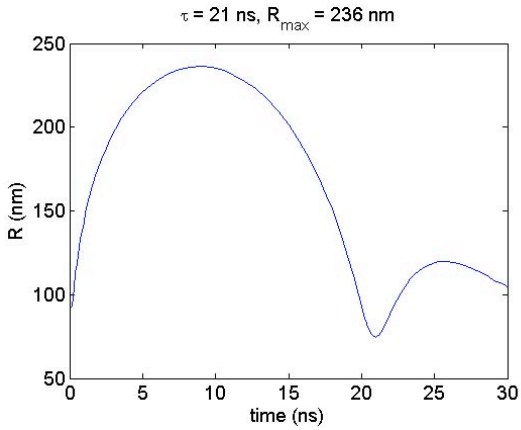

Figure 12. Radius time curve of the cavitation bubble produced by a single femtosecond laser pulse focused at NA = 1.3 that leads to a peak temperature of T_{max} = 200 °C at the focus center. For the calculations, isothermal conditions for the bubble content with respect to the surrounding liquid were assumed.

$$E_B = (4\pi/3)[(p_\infty - p_v) + p_\sigma]R_{\max}^3 \tag{11}$$

of the expanded bubble. Here $p_\sigma = \sigma/2R$ denotes the pressure the pressure exerted by the surface tension at the bubble wall. For the sake of simplicity, we neglect the time dependence of the bubble radius and use the value $p_\sigma(R_{max})$. For the case presented in Fig 12, E_B amounts to 1.1×10^{-14} J (11 femtojoule). The smallness of the bubble energy is partly explained by

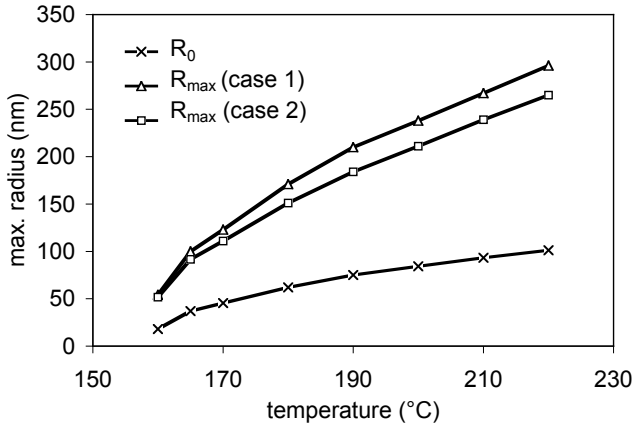

Figure 13. Maximum bubble radius R_{max} as a function of the peak temperature in the center of the focal volume, together with the radius of the nucleus, R_0. Cases 1 and 2 stand for isothermal and adiabatic conditions for the bubble content with respect to the surrounding liquid.

the small energy content of the stress transient creating the bubble. This energy equals the energy stored in thermoelastic compression of the heated fluid volume (Paltauf and Dyer, 2003),

$$E_{TE} = 1/(2\rho_0 c_0^2)\int p_0^2\, dV\,, \tag{12}$$

where p_0 is the thermoelastic pressure and the integration encompasses the entire volume heated by the laser pulse. For a temperature rise in the center of the focal volume of 180°C (Fig. 12) that leads to a maximum pressure p_0 of 221 MPa, E_{TE} amounts to 7.8 _ 10^{-14} J. The total heat content of the plasma is

$$E_{tot} = \rho_0 C_p \int \Delta T\, dV\,, \tag{13}$$

giving E_{tot} = 1.66 _ 10^{-11} J under the same conditions. The energetic conversion efficiency from heat into the thermoelastic wave is thus E_{TE}/E_{tot} = 0.46%, and the conversion from thermoelastic energy into bubble energy is 14.1%.

This result of a low conversion efficiency from absorbed laser energy into mechanical energy for femtosecond pulses (0.065%) is supported by experimental results (Noack et al., 1998b, Vogel et al., 1999). By contrast, for nanosecond optical breakdown with NA = 0.9 the conversion efficiency was experimentally found to be 12.7 % for λ = 1064 nm, and 3.3% for λ = 532 nm at the breakdown threshold, and it reached values of 53% and 33.5 %, respectively, for energies 10-fold above threshold (Venugopalan et al., 2002).

6.4.1 Experimental data on cavitation bubble dynamics

Results of time-resolved investigations of the effects of transient femtosecond-laser-induced bubbles on cells are not yet available. However, Dayton et. al. (2001) investigated the oscillations of 1.5-μm radius bubbles that were phagocytosed by leukocytes and stimulated by a rarefaction-first one-cycle acoustic pulse with 440 ns duration. By means of streak photography and high-speed photography with 100 Mill. f/s they observed that phagocytosed bubbles expanded about 20-45% less than free microbubbles in response to a single acoustic pulse of the same intensity. The difference is due to the viscosity of the cytoplasm and the elastic modulus of the cytoskeleton. Bubbles subjected to a tensile stress amplitude of 0.9 MPa expanded to a radius of 6 μm without rupturing the cell membrane. Larger oscillations caused immediate cell lysis. The viability of the non-lysed cells after insonation was not tested, but it is evident that the bubble oscillations strain the cell membrane and deform or even rupture the cytoskeleton. In the case of femtosecond optical breakdown, the radius of the bubble nucleus is much smaller (≈ 90 nm

compared to 1.5 μm), and the tensile stress transient acting on the bubbles is much shorter than in the case investigated by Dayton (≈ 100 ps compared to 220 ns). Therefore, the resulting bubbles cause little structural damage within a cell and do not affect cell viability.

Lin et. al. (1999) and Leszczynski et al. (2001) investigated the thresholds for cell death produced by cavitation induced around absorbing microparticles irradiated by nanosecond laser pulses. They observed that an energy of 3 nJ absorbed by a single particle of 1 μm diameter produced sufficiently strong cavitation to kill a trabecular meshwork cell after irradiation with a single laser pulse. Pulses with 1 nJ absorbed energy produced lethality after several exposures (Lin et al., 1999). Viability was lost even when no morphologic damage was apparent immediately after the collapse of the transient bubble with less than 1 μs life time, corresponding to $R_{max} \leq 5.5$ μm). Nuclear staining of nonviable cells by ethidium bromide confirmed that cell death was associated with membrane damage. According to Neumann and Brinkmann (2005b), a bubble radius of 3 μm within a cell of 7.5 μm radius is sufficient to cause an enlargement of the membrane by 4% that will result in membrane rupture (Needham and Nunn, 1990, Boal, 2002). The results of our calculations in Fig. 20 demonstrate that the radius of fs-laser-produced transient bubbles remains well below this damage threshold. This applies even for laser pulse energies of a few nanojoule because for $\rho_{cr} = 10^{21}$ cm^{-3} and 1 μm plasma length about 99% of the incident energy is transmitted through the focal region (Noack and Vogel, 1999). The heated volume is much smaller than the volume of the microparticles investigated by Lin et. al. (1999), and the deposited heat energy corresponding to a peak temperature of $T_{max} = 200$°C or 300 °C is only 16.6 or 25.8 pJ, respectively, much less than in Lin's case.

Bubbles around gold nanoparticles are of interest in the context of nanoparticle cell surgery (section 1.1). When particles with 4.5 nm radius were irradiated by 400-nm, 50-fs pulses, bubbles of up to 20 nm radius were observed by X-ray scattering (Kotaidis and Plech, 2005). The small size of these bubbles which is one order of magnitude less than for those produced by focused fs pulses is consistent with the fact that the collective action of a large number of nanoparticles is required to produce the desired surgical effect.

The transient bubbles produced by single laser pulses can only be detected by very fast measurement schemes. However, during high-repetition rate pulse series accumulative thermal effects and chemical dissiciation of biomolecules come into play (sections 4 and 5.2) that can produce long-lasting bubbles, which are easily observable under the microscope König et al., 2002, Supatto et al., 2005a,b, Riemann et al., 2005). Even though thermoelastic forces may still support the bubble growth, it is mainly driven by chemical or thermal decomposition of biomolecules into small volatile fragments and by boiling of cell water. After the end of the fs pulse train, the vapor will rapidly

condense but the volatile decomposition products will disappear only by dissolution into the surrounding liquid and thus form a longer-lasting bubble.

7 IMPLICATIONS FOR LASER EFFECTS ON BIOLOGICAL CELLS AND TISSUES

Two parameter regimes have been established for femtosecond laser nanosurgery: One technique uses long pulse series from fs oscillators with repetition rates in the order of 80 MHz and pulse energies well below the optical breakdown threshold (König et al., 1999, 2001, Smith et al., 2001, Tirlapur and König, 2002, Zeira et al., 2003, Saccioni et al., 2005, Supatto et al., 2005a,b, Riemann et al., 2005, König et al., 2005). From 40000 pulses (König et al., 1999) to several million pulses (Tirlapur et al., 2002, Saccioni et al., 2005) have been applied at one specific location to achieve the desired dissection or membrane permeabilisation. The other approach uses amplified pulse series at 1 kHz repetition rate with pulse energies slightly above the threshold for transient bubble formation (Yanik et al., 2004, Watanabe et al., 2004, Watanabe et al., 2005, Heisterkamp et al., 2005, Maxwell et al., 2005). Here the number of pulses applied at one location varied between thirty (Watanabe et al., 2004) and several hundred (Yanik et al., 2004, Heisterkamp et al., 2005, Maxwell et al., 2005).

Based on the discussion of the physical effects associated with femtosecond laser induced plasma formation in the previous sections, we now proceed to explain the working mechanisms of both modalities for cell surgery. For this purpose, the different low-density plasma effects and physical breakdown phenomena are summarized in Fig. 14, together with experimental damage, transfection and dissection thresholds on cells. The different effects are scaled by the corresponding values of free-electron density and irradiance. Chemical cell damage (2) refers to membrane dysfunction and DNA strand breaks leading to apoptosis-like cell death observed after scanning irradiation of PtK2 cells with 800-nm pulses at 80 MHz repetition rate (Tirlapur et al., 2001). Chromosome dissection (3) relates to the intranuclear chromosome dissection (König et al., 1999), and (4) to cell transfection by transient membrane permeabilisation (König and Tirlapur, 2002), both performed using 80-MHz pulse trains from a femtosecond oscillator. Mitochondrion ablation (8) refers to the ablation of a single mitochondrion in a living cell using 1-kHz pulse trains (Shen et al., 2005), and axon dissection (9) applies to axotomy in life C-elegans worms carried out with sequences of pulses emitted at 1 kHz repetition rate from a regenerative amplifier (Yanik et al., 2004. Points (1), (5), (6) and (7) stand for physical events or threshold criteria.

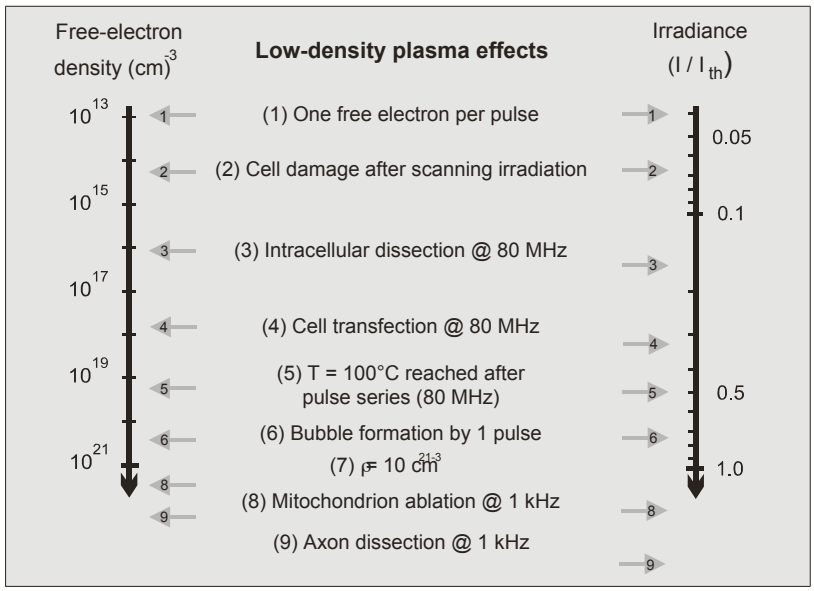

Figure 14. Overall view of physical breakdown phenomena induced by femtosecond laser pulses, together with experimental damage, transfection and dissection thresholds on cells, scaled by .free-electron density and irradiance. The irradiance values are normalized to the optical breakdown threshold I_{th} defined by $\rho_{cr} = 10^{21}$ cm^{-3}. All data refer to plasma formation in water with femtosecond pulses of about 100 fs pulses and 800 nm wavelength.

7.1 Pulse trains at MHz repetition rates with energies below the threshold for bubble formation

The irradiance threshold (2) for cell death induced by laser pulse series of 80 MHz repetition rate scanned over the entire cell volume ($0.067\times I_{rate}$) is lower than the irradiance threshold for intracellular dissection (3). However, this does not imply that intracellular dissection with 80-MHz pulse series must lead to severe cell damage because locally confined irradiation does not affect cell viability in the same way as scanning irradiation.

The threshold for intranuclear chromosome dissection with 80-MHz pulse series (3) is almost 4 times as large as the irradiance (1) producing one free electron per pulse in the focal volume ($0.15\times I_{rate}$ vs $0.04\times I_{rate}$). In fact, about 1000 free electrons per pulse are produced with the parameters used for dissection. Therefore, it is very likely that the intracellular ablation produced by long trains of femtosecond pulses in the low-density plasma regime relies on cumulative free-electron-mediated chemical effects. This hypothesis is supported by the facts that the individual pulses produce a thermoelastic tensile stress of only ≈ 0.014 MPa, and a pulse series of 100 μs duration results in a

temperature rise of only ≈ 0.076°C. These values for tensile stress and temperature rise are by far too small to cause any cutting effect or other types of cell injury. The breaking of chemical bonds, as described in section 4, may first lead to a disintegration of the structural integrity of biomolecules and finally to a dissection of subcellular structures. Bond breaking may be initiated both by resonant interactions with low-energy electrons, and by multiphoton processes of lower order that do not yet create free electrons (König et al., 1999, Koester et al., 1999, Hopt et al., 2001, Eggeling et al., 2005).

Interestingly, transient membrane permeabilisation for gene transfer (4) requires a considerably larger laser dose than chromosome dissection. Not only the irradiance is larger, but the number of applied pulses (≈ 10^6) also exceeds by far the quantity necessary for chromosome dissection (≈ 4×10^4). Chromosome dissection may be facilitated by the DNA absorption around 260 nm enabling nonlinear absorption through lower-order multiphoton processes. Moreover, while breakage of relatively few bonds is sufficient for chromosome dissection, the creation of a relatively large opening is required for diffusion of a DNA plasmid through the cell membrane. The corresponding laser parameters are still within the regime of free-electron-mediated chemical effects but already quite close to the range where cumulative heat effects start to play a role (5).

At larger laser powers, bubbles with a lifetime in the order of a few seconds were observed that probably arise from dissociation of biomolecules into volatile, non-condensable fragments (König et al., 2002, Masters et al., 2004, Supatto et al., 2005a,b, Riemann et al., 2005). As discussed in section 6.4, this dissociation of relatively large amounts of biomaterials can be attributed both to free-electron-chemical and photochemical bond breaking as well as to accumulative thermal effects. The appearance of the bubbles is an indication of severe cell damage or cell death within the targeted region and defines an upper limit for the laser power suitable for nanosurgery. A criterion for successful intratissue dissection at lower energy levels is the appearance of intense autofluorescence in perinuclear cell regions (König et al., 2002, Supatto et al., 2005a,b) that is likely due to the destruction of mitochondria at the rim of the laser cut (Oehring et al., 2000).

7.2 Pulses at kHz repetition rates with energies above the bubble formation threshold

When pulse trains of 1 kHz repetition rate are employed for nanosurgery, pulse energies ranging from 2-40 nJ are used (Yanik et al., 2004, Watanabe et al., 2004, Shen et al., 2005, Heisterkamp et al., 2005). Examples are the ablation of single mitochondria (8) by several hundred 2-nJ pulses (Shen et al., 2005), and the severing of axons in a live C-elegans worm (9) with a similar

number of 10-nJ pulses (Yanik et al., 2004). These energies are above the threshold for thermoelastically induced formation of minute transient cavitation bubbles (6), and are thus associated with mechanical disruption effects. The tensile thermoelastic stress waves enable dissection of cellular structures at low volumetric energy densities, and the small size of the heated volume (Fig. 8) correlates with a radius of the expanded bubble in the order of only 120-300 nm (Fig. 20). This explains why fs-laser induced bubble formation does not necessarily lead to cell damage whereas ns-laser-induced bubble generation is usually associated with cell death (Lin et al., 1999, Leszczynski et al., 2001, Pitsillides et al., 2003, Roegener et al., 2004, Neumann and Brinkmann, 2005b).

Due to the contribution of mechanical effects to dissection, the total energy required for nanosurgery with kHz pulse series is less than necessary with MHz pulse trains. For example, ablation of a mitochondrion using 1-kHz pulses required a total energy of less than 1 μJ (Shen et al., 2005), while for intranuclear chromosome dissection with 80-MHz pulses an energy of 15 μJ was needed (König et al., 1999).

For sufficiently large pulse energies, bubble expansion and shock wave pressure can cause effects far beyond the focal volume which lead to cell death (Wtanabe et al., 2004, Watanabe, 2005, Zohdy et al., 2005). To avoid unwanted side effects, irradiances should be used that are only slightly above the bubble formation threshold. Useful techniques for an on-line monitoring of the ablation threshold during laser surgery are to detect the onset of photobleaching, or of light scattering by bubbles generated at the laser focus. Heisterkamp et. al. (2005) found that the threshold for photobleaching is just below the ablation threshold. Neumann and Brinkmann (2005a) described a light scattering technique for an on-line detection of micrometer-sized bubbles produced by pulsed laser irradiation.

We conclude that, depending on the repetition rate of the fs laser pulses, nanosurgery relies on two very different mechanisms. With MHz repetition rates, dissection is due to accumulative chemical effects in low-density plasmas. In this regime, no transient bubbles with submicrosecond lifetime are produced, and the formation of long-lived bubbles by accumulative chemical and thermal effects must be avoided. With pulse trains at kHz repetition rate, the accumulative creation of chemical effects would take too long to be practical. Therefore, pulse energies are raised to a level where the thermoelastic generation of minute transient bubbles enables nanosurgery. Due to their short lifetime of less than 100 ns and the long time intervals between the laser pulses, no cumulative bubble growth occurs as long as pulse energies close to the bubble formation threshold are used. Both modes of femtosecond-laser nanoprocessing can achieve a 2-3 fold better precision than cell surgery using cw irradiation, and enable manipulation at arbitrary locations.

Acknowledgement

This work was sponsored by the US Air Force Office of Scientific Research through its European Office of Aerospace Research and Development under grant number FA8655-02-1-3047, and, in parts, by the German Bundesministerium für Bildung und Forschung under grant number 13N8461.

REFERENCES

Ammosov, M.V., Delone, N. B., and Krainov, V. P., 1986, Tunnel ionization of complex atoms and of atomic ions in an alternating electromagnetic field, *Sov. Phys. JETP* **64**, 1191-1194.

Amy, R. L., and Storb, R., 1965, Selective mitochondrial damage by a ruby laser microbeam: an electron microscopic study, *Science* **150**, 756-758.

Arnold, C. L., Heisterkamp, A., Ertmer, W. and Lubatschowski, H., 2005, Streak formation as side effect od optical breakdown during processing the bulk of transparent Kerr media with ultrashort laser pulses, *Appl. Phys. B* **80**, 247-253.

Arnold, D., and Cartier, E., 1992, Theory of laser-induced free-electron heating and impact ionization in wide-band-gap solids, *Phys. Rev. B* **46**, 15102-15115.

Barnes, P. A., and Rieckhoff, K. E., 1968, Laser induced underwater sparks. *Appl. Phys. Lett.* **13**, 282-284.

Berns, M. W., Olson, R. S., and Rounds, D. E., 1969, In vitro production of chromosomal lesions with an argon laser microbeam, *Nature* **221**, 74-75.

Berns, M. W., Cheng, W. K., Floyd, A. D. and Ohnuki, Y., 1971, Chromosome lesions produced with an argon laser microbeam without dye sensitization, *Science* **171**, 903-905.

Berns, M. W., Aist, J., Edwards, J., Strahs, K., Girton, J., McNeil, P., Kitzes, J. B., Hammer-Wilson, M., Liaw, L.-H., Siemens, A., Koonce, M., Peterson, S., Brenner, S., Burt, J., Walter, R., Bryant, P. J., van Dyk, D., Coulombe, J., Cahill, T. and Berns, G. S., 1981, Laser Microsurgery in cell and developmental biology, *Science* **213**, 505-513.

Bessis, M., and Nomarski, G., 1960, Irradiation ultra-violette des organites cellulaires avec observation continue en contraste en phase, *J. Biophys. Biochem. Cytol.* **8**, 777-792.

Bessis, M., Gires, F., Mayer, G., and Nomarski, G., 1962, Irradiation des organites cellulaires à l'aide d'un laser à rubis, *C. R. Acad. Sci.III - Vie* **255**, 1010.

Bessis, M., 1971, Selective destruction of cell organelles by laser beam. Theory and practical applications, *Adv. Biol. Med. Phys.* **13**, 209-213.

Bloembergen, N., 1974, Laser-induced electric breakdown in solids, *IEEE J. Quantum Electr.* **QE-10**, 375-386.

Boal, D., 2002, *Mechanics of the cell*, Cambridge Univ. Press, Cambridge, UK.

Born, M., and Wolf, E., 1970, *Principles of Optics*, Pergamon Press, Oxford, 1970.

Botvinick, E. L., Venugopalan, V., Shah, J. V., Liaw, L. H., and Berns, M., 2004, Controlled ablation of microtubules using a picosecond laser, *Biophys. J.* **87**, 4203-4212.

Boudaiffa, B., Cloutier, P., Hunting, D., Huels, M. A., and Sanche, L., 2000, Resonant formation of DNA strand breaks by low-energy (3 to 20 eV) electrons, *Science* **287**, 1658-1660.

Chapyak, E. J., Godwin, R. P., and Vogel, A., 1997, A comparison of numerical simulations and laboratory studies of shock waves and cavitation bubble growth produced by optical breakdown in water, *Proc. SPIE* **2975**, 335-342.

Chung, S. H., Clark, D. A., Gabel, C. V., Mazur, E., and Samuel, A. D. T., 2005, Mapping thermosensation to a dendrite in C. elegans using femtosecond laser dissetion, *J. Neurosci.* **25** (at press)

Colombelli, J., Grill, S. W., and Stelzer, E. H. K., 2004, Ultraviolett diffraction limited nanosurgery of live biological tissues, *Rev. Sci. Instrum.* **75**, 472-478.

Colombelli, J., Reynaud, and Stelzer, E. H. K., 2005a, Subcellular nanosurgery with a pulsed subnanosecond UV-A laser, *Med. Laser Appl.* **20,** 217-222.

Colombelli, J., Reynaud, E. G., Rietdorf, J., Pepperkork, R., and Stelzer, E. H. K., 2005b, Pulsed UV laser nanosurgery: retrieving the cytoskeleton dynamics in vivo, *Traffic* **6,** 1093-1102.

Cox, B. T., and Beard, P. C., 2005, Fast calculation of pulsed photoacoustic fields in fluids using k-space methods, *J. Acoust. Soc. Am.* **117**, 3616-3627.

Dayton, P. A., Chomas, J. E., Lunn, A. F. H., Allen, J. S., Lindner, J. R., Simon, S. I., and Ferrara, K. W., 2001, Optical and acoustical dynamics of microbubble contrast agents inside neutrophils, *Biophys. J.* **80**, 1547-1556.

Debenedetti, P. G., 1996, *Metastable Liquids: Concepts and Principles*, Princeton University Press, Princeton.

Ditlbacher, H., Krenn, J. R., Leitner, A., and Aussenegg, F. R., 2004, Surface plasmon polariton based optical beam profiler, *Opt. Lett.* **29**, 1408-1410.

Docchio, F., Sachhi, C. A., and Marshall, J., 1986, Experimental investigation of optical breakdown thresholds in ocular media under single pulse irradiation with different pulse durations, *Lasers Ophthalmol*. **1**, 83-93.

Du, D., Squier, J., Kurtz, R., Elner, V., Liu, X., Güttmann, G., and Mourou, G., 1994, Damage threshold as a function of pulse duration in biological tissue, in P. F. Barbara, W. H. Knox, G. A. Mourou, and A. H. Zewail *Ultrafast Phenomena IX,* Springer, New York, pp. 254-255.

Du, D., Liu, X., and Mourou, G., 1996, Reduction of multi-photon ionization in dielectrics due to collisions, *Appl. Phys. B* **63**, 617-621.

Eggeling, C., Volkmer, A., and Seidel, C. A. M., 2005, Molecular photobleaching kinetics of Rhodamine 6G by one- and two-photon induced confocal fluorescence microscopy, *Chem. Phys. Chem.* **6**, 791-804.

Fan, C. H., Sun, J., and Longtin, J. P., 2002a, Breakdown threshold and localized electron density in water induced by ultrashort laser pulses, *J. Appl. Phys.* **91**, 2530-2536.

Fan, C. H., Sun, J., and Longtin, J. P., 2002b, Plasma absorption of femtosecond laser pulses in dielectrics, *J. Heat Transf. – T. ASME* **124**, 275-283.

Feit, M. D., Komashko, A. M., and Rubenchik, A. M., 2004, Ultra-short pulse laser interaction with transparent dielectrics, *Appl. Phys. A* **79**, 1657-1661.

Feng, Q., Moloney, J. V., Newell, A. C., Wright, E. M., Cook, K., Kennedy, P. K., Hammer, D. X., Rockwell, B. A., and Thompson, C. R., 1997, Theory and simulation on the threshold of water breakdown induced by focused ultrashort laser pulses, *IEEE J. Quantum Electron.* **33**, 127-137.

Garret, B. C., et al., 2005, Role of water in electron-initiated processes and radical chemistry; issues and scientific advances, *Chem Rev.* **105**, 355-389.

Garrison, B., Itina, T. E., and Zhigilei, L. V., 2003, Limit of overheating and the threshold behavior in laser ablation. *Phys. Rev. E* **68**, 041501.

Garwe, F., Csáki, A., Maubach, G., Steinbrück, A., Weise, A., König, K., Fritsche, W., 2005, Laser pulse energy conversion on sequence-specifically bound metal nanoparticles and its application for DNA manipulation, *Med. Laser Appl.* **20**, 201-206.

Gilmore, F. R., 1952, Calif. Inst. Techn. Rep. **26-4**.

Gohlke, S., and Illenberger, E., 2002, Probing biomolecules: Gas phase experiments and biological relevance, *Europhys. News* **33**, 207-209.

Grand, D., Bernas, A., and Amouyal, E., 1979, Photoionization of aqueous indole; conduction band edge and energy gap in liquid water, *Chem. Phys.* **44**, 73-79.

Greulich, K. O., 1999, *Micromanipulation by Light in Biology and Medicine,* Birkhäuser, Basel, Boston, Berlin, 300pp.

Grill, S. W., Howard, J., Schäffer, E., Stelzer, E. H. K. and Hyman, A. A., 2003, The distribution of active force generators controls mitotic spindle position, *Science* **301**, 518-521.

Grill, S., and Stelzer, E. H. K., 1999, Method to calculate lateral and axial gain factors of optical setups with a large solid angle, *J. Opt. Soc. Am. A* **16**, 2658-2665.

Hammer, D. X., Thomas, R. J., Noojin, G. D., Rockwell, B. A., Kennedy, P. A., and Roach, W. P., 1996, Experimental investigation of ultrashort pulse laser-induced breakdown thresholds in aqueous media, *IEEE J. Quantum Electr.* **QE-3**, 670-678.

Hammer, D. X., Jansen, E. D., Frenz, M., Noojin, G. D., Thomas, R. J., Noack, J., Vogel, A., Rockwell, B. A., and Welch, A. J., 1997, Shielding properties of laser-induced breakdown in water for pulse durations from 5 ns to 125 fs, *Appl. Opt.* **36**, 5630-5640.

Han, M., Zickler, L., Giese, G., Walter, M., Loesel, F. H., and Bille, J. F., 2004, Second-harmonic imaging of cornea after intrastromal femtosecond laser ablation, *J. Biomed. Opt.* **9**, 760-766.

Heisterkamp, A., Ripken, T., Lubatschowski, H., Mamom, T., Drommer, W., Welling, H., and Ertmer, W., 2002, Nonlinear side-effects of fs-pulses inside corneal tissue during photodisruption, *Appl. Phys. B* **74**, 419-425.

Heisterkamp, A., Mamom, T., Kermani, O., Drommer, W., Welling, H., Ertmer, W., and Lubatschowski, H., 2003, Intrastromal refractive surgery with ultrashort laser pulses: in vivo study on the rabbit eye, *Graefes Arch. Clin. Exp. Ophthalmol.* **241**, 511-517.

Heisterkamp, A., Maxwell, I. Z., Mazur, E., Underwood, J. M., Nickerson, J. A., Kumar, S. and Ingber, D. E., 2005, Pulse energy dependence of subcellular dissection by femtosecond laser pulses, *Opt. Expr.* **13**, 3690-3696.

Hopt, A., and Neher, E., 2001, Highly nonlinear photodamage in two-photon fluorescence microscopy, *Biophys. J.* **80**, 2029-2036.

Hotop, H., 2001, Dynamics of low energy electron collisions with molecules and clusters, in: L.G. Christophorou, J.K. Olthoff (eds.): *Proc. Int. Symp. on Gaseous Dielectrics IX 22-25 May 2001, Ellicott City, MD, USA*, Kluwer Academic/Plenum Press, New York, pp. 3-14.

Huels, M. A., Boudaiffa, B., Cloutier, P., Hunting, D., and Sanche, L., 2003, Single, double, and multiple double strand breaks induced in DNA by 3-100 eV electrons, *J. Am. Chem. Soc.* **125**, 4467-4477.

Huettmann, G. and Birngruber, R., 1999, On the possibility of high-precision photothermal microeffects and the measurement of fast thermal denaturation of proteins, *IEEE J. Sel. Topics Quantum Electron.* **5**, 954-962.

Jay, D. G., and Sakurai, T., 1999, Chromophore-assisted laser inactivation (CALI) to elucidate cellular mechanisms of cancer, *Biochim. Biophys. Acta* **1424**, M39-M48.

Joglekar, A. P., Liu, H., Meyhöfer, E., Mourou, G., and L. Hunt, A., 2004, Optics at critical intensity. Applications to nanomorphing, *Proc. Nat. Acad. Sci.* **101**, 5856-5861.

Juhasz, T., Loesel, F. H., Kurtz, R. M., Horvath, C., Bille, J. F., and Mourou, G., 1999, Corneal refractive surgery with femtosecond lasers, *IEEE J. Sel. Topics Quantum Electron.* **5**, 902-910.

Kaiser, A., Rethfeld, B., Vicanek, M., and Simon, G., 2000, Microscopic processes in dielectrics under irradiation by subpicosecond pulses, *Phys. Rev. B* **61**, 11437-11450.

Kasparian, J., Solle, J., Richard, M., and Wolf, J.-P., 2004, Ray-tracing simulation of ionization-free filamentation, *Appl. Phys. B.* **79**, 947-951.

Keldysh, L. V., 1960, Kinetic theory of impact ionization in semiconductors, *Sov. Phys. JETP* **11**, 509-518.

Keldysh, L. V., 1965, Ionization in the field of a strong electromagnetic wave, *Sov. Phys. JETP* **20**, 1307-1314.

Kennedy, P. K., 1995, A first-order model for computation of laser-induced breakdown thresholds in ocular and aqueous media: Part I – Theory, *IEEE J. Quantum Electron.* **QE-31**, 2241-2249.

Kennedy, P. K., Hammer, D. X., and Rockwell, B. A., 1997, Laser-induced breakdown in aqueous media, *Progr. Quantum Electron.* **21**, 155-248.

Kiselev, S. B., 1999, Kinetic boundary of metastable states in superheated and stretched liquids, *Physica A* **269**, 252-268.

Knapp, R. T., Daily, J. W., and Hammitt, F. G., 1971, *Cavitation*, McGraw-Hill, New York, 1971, pp. 117-131.

Koester, H. J., Baur, D., Uhl, R., and Hell, S. W., 1999, Ca^{2+} fluorescence imaging with pico- and femtosecond two-photon excitation: signal and photodamage, *Biophys. J.* **77**, 2226-2236.

Kolesik, M., Wright, E. M., and Moloney, J. V., 2004, Dynamic nonlinear X-waves for femtosecond pulse propagation in water, *Phys. Rev. Lett.* **92**, 253901.

König, K., Riemann, I., Fischer, P., and Halbhuber, K., 1999, Intracellular nanosurgery with near infrared femtosecond laser pulses, *Cell. Mol. Biol.* **45**, 195-201.

König, K., Riemann, I., and Fritsche, W., 2001, Nanodissection of human chromosomes with near-infrared femtosecond laser pulses, *Opt. Lett.* **26**, 819-821.

König, K., Krauss, O., and Riemann, I., 2002, Intratissue surgery with 80 MHz nanojoule femtosecond laser pulses in the near infrared, *Opt. Express* **10**, 171-176.

König, K., Riemann, I., Stracke, F., and Le Harzic, R., 2005, Nanoprocessing with nanojoule near-infrared femtosecond laser pulses, *Med. Laser Appl.* **20**, 169-184.

Köstli, K. P., Frenz, M., Bebie, H., and Weber, H. P., 2001, Temporal Backward Projection of Optoacoustic Pressure Transients Using Fourier Transform Methods, *Physics in Medicine and Biology* **46,** 1863-1872.

Kotaidis, V., and Plech, A., 2005, Cavitation dynamics on the nanoscale, *Appl. Phys. Lett.* **87**, 213102.

Krasieva, T. B., Chapman, C. F., LaMorte, V. J., Venugopalan, V., Berns, M. W. and Tromberg, B. J., 1998, Cell permeabilization and molecular transport by laser microirradiation, *Proc. SPIE* **3260**, 38-44.

Lenzner, M., Krüger, J., Sartania, S., Cheng, Z., Spielmann, Ch., Mourou, G., Kautek, W., and Krausz, F., 1998, Femtosecond optical breakdown in dielectrica, *Phys. Rev. Lett.* **80**, 4076-4079.

Leszczynski, D., Pitsillides, C. M., Pastila, R. K., Anderson, R. R., and Lin, C. P., 2001, Laser-beam triggered microcavitation : a novel method for selective cell destruction, *Radiat. Res.* **156**, 399-407.

Liang, H., Wright, W. H., Cheng, S., He, W., and Berns, M. W., 1993, Micromanipulation of chromosomes in PTK2 cells using laser microsurgery (optical scalpel) in combination with laser-induced optical force (optical tweezers), *Exp. Cell Res.* **204**, 110-120.

Lin, C. P., Kelly, M. W., Sibayan, S. A. B., Latina, M. A., and Anderson, R. R., 1999, Selective cell killing by microparticle absorption of pulsed laser radiation, *IEEE J. Sel. Top. Quantum Electron.* **5**, 963-968.

Liu, W., Kosareva, O., Golubtsov, I. S., Iwasaki, A., Becker, A., Kandidov, V. P. and Chin, S. L., 2003, Femtosecond laser pulse fiolamentation versus optical breakdown in H_2O, *Appl. Phys. B* **76**, 215-229.

Mao, S. S., Quéré, F., Guizard, S., Mao, X. Russo, R. E., Petite, G., and Martin, P., 2004, Dynamics of femtosecond laser interactions with dielectrics, *Appl. Phys. A* **79**, 1695-1709.

Masters, B. R., So, P. T. C., Buehler, C., Barry, N., Sutin, J. D., Mantulin, W. W., and Gratton, E., 2004, Mitigating thermal mechanical damage potential during two-photon dermal imaging, *J. Biomed. Opt.* **9**, 1265-1270.

Maxwell, I., Chung, S., and Mazur, E., 2005, Nanoprocessing of subcellular targets using femtosecond laser pulses, *Med. Laser Appl.* **20**, 193-200.

Meier-Ruge, W., Bielser, W., Remy, E., Hillenkamp, F., Nitsche, R., and Unsöld, R., 1976, The laser in the Lowry technique for microdissection of freeze-dried tissue slices, *Histochem J.* **8**, 387–401.

Meldrum, R. A., Botchway, S. W., Wharton, C. W., and Hirst, G. J., 2003, Nanoscale spatial induction of ultraviolet photoproducts in cellular DNA by three-photon near-infrared absorption, *EMBO Rep.* **12**, 1144-1149.

Minoshima, K., Kowalevicz, A. M., Hartl, I., Ippen, E., and Fujimoto, J. G., 2001, Photonic device fabrication in glass by use of nonlinear materials processing with a femtosecond laser oscillator, *Opt. Lett*. **26,** 1516-1518.

Nahen, K., and Vogel, A., 1996, Plasma formation in water by picosecond and nanosecond Nd:YAG laser pulses - Part II: Transmission, scattering, and reflection, *IEEE J. Selected Topics Quantum Electron.* **2**, 861-871.

Needham, D., and Nunn, R. S., 1990, Elastic deformation and failure of liquid bilayer membranes containing cholesterol, *Biophys. J.* **58**, 997-1009.

Neumann, J., and Brinkmann, R., 2005a, Boiling nucleation on melanosomes and microbeads transiently heated by nanosecond and microsecond laser pulses, *J. Biomed. Opt.* **10**, 024001.

Neumann, J. and Brinkmann, R., 2005b, Nucleation and dynamics of bubbles forming around laser heated microabsorbers, *Proc. SPIE* **5863**, 586307, 1-9.

NIST, 2005, National Institute of Standards Chemistry Web Book, Thermophysical Properties of Fluid Systems, http://webbook.nist.gov/chemistry/fluid/

Niyaz, Y., and Sägmüller, B., 2005, Non-contact laser microdissection and pressure catapulting: Automation via object-oriented image processing, *Med. Laser Appl.* **20**, 223-232.

Nikogosyan, D. N., Oraevsky, A. A., and Rupasov, V., 1983, Two-photon ionization and dissociation of liquid water by powerful laser UV radiation, *Chem. Phys.* **77**, 131-143.

Noack, J., and Vogel, A., 1998a, Single shot spatially resolved characterization of laser-induced shock waves in water, *Appl. Opt*. **37**, 4092-4099.

Noack, J., Hammer, D. X., Noojin, G. D., Rockwell, B. A., and Vogel, A., 1998b, Influence of pulse duration on mechanical effects after laser-induced breakdown in water, *J. Appl. Phys*. **83**, 7488-7495.

Noack, J., 1998c, *Optischer Durchbruch in Wasser mit Laserpulsen zwischen 100 ns und 100 fs*, PhD Dissertation, University of Lübeck, Lübeck, 237 pp..

Noack, J., and Vogel, A., 1999, Laser-induced plasma formation in water at nanosecond to femtosecond time scales: Calculation of thresholds, absorption coefficients, and energy density, *IEEE J. Quantum Electron.* **35**, 1156-1167.

Nolte, S., Momma, C., Jacobs, H., Tünnermann, A., Chikov, B. N., Wellegehausen, B., and Welling, H., 1997, Ablation of metals by ultrashort laser pulses, *J. Opt. Soc. Am. B* **14**, 2716-2722.

Oehring, H., Riemann, I., Fischer, P., Halbhuber, K. J., and König, K., 2000, Ultrastructure and reproduction behavior of single CHO-K1 cells exposed to near-infrared femtosecond laser pulses, *Scanning* **22**, 263-270.

Oraevsky, A. A., Da Silva, L. B., Rubenchik, A. M., Feit, M. D., Glinsky, M. E., Perry, M. D. Mammini, B. M., Small IV, W., and Stuart, B., 1996, Plasma mediated ablation of biological tissues with nanosecond-to-femtosecond laser pulses: relative role of linear and nonlinear absorption, *IEEE J. Sel. Top. Quantum Electron.* **2**, 801-809.

Paltauf, G., and Schmidt-Kloiber, H., 1996, Microcavity dynamics during laser-induced spallation of liquids and gels, *Appl. Phys. A* **62**, 303-311.

Paltauf, G. and Schmidt-Kloiber, H., 1999, Photoacoustic cavitation in spherical and cylindrical absorbers, *Appl. Phys. A* **68**, 525-531.

Paltauf, G. and Dyer, P., 2003, Photomechanical processes and effects in ablation, *Chem Rev.* **103**, 487-518.

Paterson, L., Agate, B., Comrie, M., Ferguson, R., Lake, T. K., Morris, J. E., Carruthers, A. E., Brown, C. T. A., Sibbett, W., Bryant, P. E., Gunn-Moore, F., Riches, A. C. and Dholakia, K., 2005, Photoporation and cell transfection using a violet diode laser, *Opt. Express* **13**, 595-600.

Pitsillides, C. M., Joe, E. K., Wei, X., Anderson, R. R., and Lin, C. P., 2003, Selective cell targeting with light absorbing microparticles and nanoparticles, *Biophys. J.* **84**, 4023-4032.

Ratkay-Traub, I., Ferincz, I. E., Juhasz, T., Kurtz, R. M., and Krueger, R. R., 2003, First clinical results with the femtosecond neodymium-glass laser in refractive surgery, *J. Refract. Surg.* **19**, 94-103.

Rayner, D. M., Naumov, A., and Corkum, P. B., 2005, Ultrashort pulse non-linear optical absorption in transparent media, *Opt. Expr.* **13**, 3208-3217.

Rethfeld, B., 2004, Unified model for the free-electron avalanche in laser-irradiated dielectrics, *Phys. Rev. Lett.* **92**, 187401.

Rice, M. H., and Walsh, J. M., 1957, Equation of state of water to 250 kilobars, *J. Chem. Phys.* **26**, 824-830.

Ridley, B. K., 1999, *Quantum Processes in Semiconductors*, Oxford University Press, Oxford, 436 pp..

Riemann, I., Anhut, T., Stracke, F., Le Harzic, R., and König, K., 2005, Multiphoton nanosurgery in cells and tissues. *Proc. SPIE* **5695**, 216-224.

Roegener, J., Brinkmann, R., and Lin, C. P., 2004, Pump-probe detection of laser-induced microbubble formation in retinal pigment epithelium cells, *J. Biomed. Opt*. **9**, 367-371.

Sacchi, C. A., 1991, Laser-induced electric breakdown in water, *J. Opt. Soc. Am. B*. **8**, 337-345.

Sacconi, L., Tolic-Norrelyke, I M., Antolini, R., and F. S. Pavone, 2005, Combined intracellular three-dimensional imaging and selective nanosurgery by a nonlinear microscope, *J. Biomed. Opt.* **10**, 014002.

Saul, A., and Wagner, W., 1989, A fundamental equation for water covering the range from the melting line to 1273 K at pressures up to 25 000 MPa, *J. Phys. Chem. Ref. Data* **18**, 1537-1564.

Schaffer, C. B., Brodeur, A., García, J. F., and Mazur, E., 2001, Micromachining bulk glass by use of femtosecond laser pulses with nanojoule energy, *Opt. Lett.* **26**, 93-95.

Schütze, K., and Clement-Sengewald, A., 1994, Catch and move – cut or fuse, *Nature* **368**, 667-668.

Schütze, K., and Lahr, G., 1998, Identification of expressed genes by laser-mediated manipulation of single cells, *Nat Biotechnol*. **16**, 737–742.

Schütze, K., Pösl, H., and Lahr, G., 1998, Laser micromanipulation systems as universal tools in molecular biology and medicine, *Cell. Mol. Biol.* **44**, 735-746.

Shen, N., Datta, D., Schaffer, C. B., LeDuc, P., Ingber, D. E., and Mazur, E., 2005, Ablation of cytoskeletal filaments and mitochondria in live cells using a femtosecond laser nanocissor, *MCB Mech. Chem. Biosystems* **2**, 17-25.

Shen, Y. R., 1984, *The Principles of Nonlinear Optics,* Wiley, New York, 563 pp.

Sigrist, M. W., and Kneubühl, F. K., 1978, Laser-generated stress waves in liquids, *J. Acoust. Soc. Am.* **64**, 1652-1663.

Sims, C. E., Meredith, G. D., Krasieva, T. B., Berns, M. W., Tromberg, B. J., and Allbritton, N. L., 1998, Laser-micropipet combination for single-cell analysis, *Anal. Chem.* **700**, 4570–4577.

Skripov, V. P., Sinitsin, E. N., Pavlov, P. A., Ermakov, G. V., Muratov, G. N., Bulanov N. V., and Baidakov, V. G., 1988, *Thermophysical properties of liquids in the metastable (superheated) state*, Gordon and Breach, New York, 1988.

Smith, N. I., Fujita, K., Kaneko, T., Katoh, K., Nakamura, O., Kawata, S., and S.Takamatsu, S. Generation of calcium waves in living cells by pulsed laser-induced photodisruption, *Appl. Phys. Lett.* **79**, 1208-1210.

Soughayer, J. S., Krasieva, T., Jacobson, S. C., Ramsey, J. M., Tromberg, B. C. and Albritton, N. L., 2000, Caracterization of cellular optoporation with distance, *Anal. Chem.* **72**, 1342-1347.

Steinert, R. F., and Puliafito, C. A., 1986, *The Nd:YAG Laser in Ophthalmology*, W. B. Saunders, Philadelphia, 154 pp.

Stolarski, J., Hardman, J., Bramlette, C. G., Noojin, G. D., Thomas, R. J., Rockwell, B. A., and Roach, W. P.,1995, Integrated light spectroscopy of laser-induced breakdown in aqueous media, *Proc. SPIE* **2391**, 100-109.

Stuart, B. C., Feit, M. D., Hermann, S., Rubenchik, A. M., Shore, B. W., and Perry, M. D., 1996, Nanosecond to femtosecond laser-induced breakdown in dielectrics, *Phys. Rev. B* **53**, 1749-1761.

Sun, Q., Jiang, H., Liu, Y., Wu, Z., Yang, H., and Gong, Q., 2005, Measurement of the collision time of dense electronic plasma induced by a femtosecond laser in fused silica, *Opt. Lett.* **30**, 320-322.

Supatto, W., Dèbarre, D., Moulia, B., Brouzés, E., Martin, J.-L., Farge, E., and Beaurepaire, E., 2005a, In vivo modulation of morphogenetic movements in Drosophila embryos with femtosecond laser pulses, *Proc. Nat. Acad. Sci. USA* **102**, 1047-1052.

Supatto, W., Dèbarre, D., Farge, E., and Beaurepaire, E., 2005b, Femtosecond pulse-induced microprocessing of live *Drosophila* embryos, *Med. Laser Appl.* **20**, 207-216.

Tao, W., Wilkinson, J., Stanbridge, E., and Berns, M. W., 1987, Direct gene transfer into human cultured cells facilitated by laser micropuncture of the cell membrane, *Proc. Natl. Acad. Sci. USA* **84**, 4180-4184.

Thornber, K. K., 1981, Applications of scaling to problems in high-field electronic transport, *J. Appl. Phys.* **52**, 279-290.

Tien, A. C., Backus, S., Kapteyn, H., Murnane, M., and Mourou, G., 1999, Short-pulse laser damage in transparent materials as a function of pulse duration, *Phys. Rev. Lett.* **82**, 3883-3886.

Tirlapur, U. K., König, K., Peuckert, C., Krieg, R., and Halbhuber, K.-J., 2001, Femtosecond near-infrared laser pulses elicit generation of reactive oxygen species in mammalian cells leading to apoptosis-like death, *Exp. Cell Res*. **263**, 88-97.

Tirlapur, U. K., and König, K., 2002, Targeted transfection by femtosecond laser, *Nature* **418**, 290-291.

Tschachotin, S., 1912, Die mikroskopische Strahlenstichmethode, eine Zelloperationsmethode, *Biol. Zentralbl.* **32**, 623-630.

Tsukakoshi, M., Kurata, S., Nomiya, Y., Ikawa, Y., and Kasuya, T., 1984, A novel method of DNA tranfection by laser-microbeam cell surgery, *Appl. Phys. B* **35**, 135-140.

Venugopalan, V., Guerra, A., Nahen, K., and A. Vogel, 2002, The role of laser-induced plasma formation in pulsed cellular microsurgery and micromanipulation, *Phys. Rev. Lett.* **88**, 078103, 1-4.

Vogel, A., Hentschel, W., Holzfuss, J., and W. Lauterborn, 1986, Cavitation buble dynamics and acoustic transient generation in ocular surgery with pulsed neodymium:YAG lasers, *Ophthalmology* **93**, 1259-1269.

Vogel, A., Nahen, K., and Theisen, D., 1996a, Plasma formation in water by picosecond and nanosecond Nd:YAG laser pulses - Part I: Optical breakdown at threshold and superthreshold irradiance, *IEEE J. Selected Topics Quantum Electron.* **2**, 847-860.

Vogel, A., Busch, S., and Parlitz, U., 1996b, Shock wave emission and cavitation bubble generation by picosecond and nanosecond optical breakdown in water, *J. Acoust. Soc. Am.* **100**, 148-165.

Vogel, A., Noack, J., Nahen, K., Theisen, D., Busch, S., Parlitz, U., Hammer, D. X., Nojin, G. D., Rockwell, B. A., and Birngruber, R., 1999, Energy balance of optical breakdown in water at nanosecond to femtosecond time scales. *Appl. Phys. B* **68**, 271-280.

Vogel, A., and Noack, J., 2001, Numerical simulation of optical breakdown for cellular surgery at nanosecond to femtosecond time scales, *Proc. SPIE* **4260**, 83-93.

Vogel, A., Noack, J., Hüttmann, G., and Paltauf, G., 2002, Femtosecond-laser-produced low-density plasmas in transparent biological media: A tool for the creation of chemical, thermal and thermomechanical effects below the optical breakdown threshold, *Proc. SPIE* **4633**, 23-37.

Vogel, A., and Venugopalan V, 2003, Mechanisms of pulsed laser ablation of biological tissues, *Chem Rev.* **103**, 577-644.

Vogel, A., Noack, J., Hüttmann, G., and Paltauf, G., 2005, Mechanisms of femtosecond laser nanosurgery of cells and tissues, *Appl. Phys. B* **81**, 1015-1046.

von der Linde, D., and Schüler, H., 1996, Breakdown threshold and plasma formation in femtosecond laser-solid interaction, *J. Opt. Soc. Am. B* **13**, 216-222.

Watanabe, W., Arakawa, N., Matsunaga, S., Higashi, T., Fukui, K., Isobe, K. and Itoh, K., 2004, Femtosecond laser disruption of subcellular organelles in a living cell, *Opt. Express* **12**, 4203-4213.

Watanabe, W., 2005, Femtosecond laser disruption of mitochondria in living cells, *Med. Laser Appl.***30**, 185-192.

Yanik, M. F., Cinar, H., Cinar, H. N., Chisholm, A. D., Jin, Y., and Ben-Yakar, A., 2004, Functional regeneration after laser axotomy, *Nature* **432**, 822.

Yao, C. P., Rahmanzadeh, R., Endl, E., Zhang, Z., Gerdes, J., and Hüttmann, G., 2005, Elevation of plasma membrane permeability by laser irradiation of selectively bound nanoparticles, *J. Biomed. Optics* **10**, 064012.

Zeira, E., Manevitch, A., Khatchatouriants, A., Pappo, O., Hyam, E., Darash-Yahana, M., Tavor, E., Honigman, A., Lewis, A., and Galun, E., 2003, Femtosecond infrared laser – an afficient and safe in vivo gene delivery system for prolonged expression, *Mol. Ther.* **8**, 342-350.

Zohdy, M. J., Tse, C., Ye, J. Y., and O'Donnell, M., 2005, Optical and acoustic detection of laser-generated microbubbles in single cells, *IEEE Trans. Ultrason. Ferr.* **52** (at press).